HHS Public Access

Author manuscript

Neuron. Author manuscript; available in PMC 2024 May 06.

Published in final edited form as:

Neuron. 2024 January 03; 112(1): 93–112.e10. doi:10.1016/j.neuron.2023.11.008.

Astrocyte growth is driven by the Tre1/S1pr1 phospholipid-binding G protein-coupled receptor

Jiakun Chen[1], **Tobias Stork**[1], **Yunsik Kang**[1], **Katherine A.M. Nardone**[2], **Franziska Auer**[2], **Ryan J. Farrell**[3], **Taylor R. Jay**[1], **Dongeun Heo**[1], **Amy Sheehan**[1], **Cameron Paton**[1], **Katherine I. Nagel**[3], **David Schoppik**[2], **Kelly R. Monk**[1,*], **Marc R. Freeman**[1,*]

[1]Vollum Institute, Oregon Health & Science University, Portland, OR 97239, USA

[2]Departments of Otolaryngology and Neuroscience and Physiology, Neuroscience Institute, New York University Grossman School of Medicine, New York, NY 10016, USA

[3]Neuroscience Institute, NYU Medical Center, New York, NY 10016, USA

SUMMARY

Astrocytes play crucial roles in regulating neural circuit function by forming a dense network of synapse-associated membrane specializations, but signaling pathways regulating astrocyte morphogenesis remain poorly defined. Here we show the *Drosophila* lipid-binding G protein-coupled receptor (GPCR) Tre1 is required for astrocytes to establish their intricate morphology *in vivo*. The lipid phosphate phosphatases Wunen/Wunen2 also regulate astrocyte morphology, and, via Tre1, mediate astrocyte-astrocyte competition for growth promoting lipids. Loss of *s1pr1*, the functional analog of *Tre1* in zebrafish, disrupts astrocyte process elaboration, and live-imaging and pharmacology demonstrate that S1pr1 balances proper astrocyte process extension/retraction dynamics during growth. Loss of Tre1 in flies or S1pr1 in zebrafish results in defects in simple assays of motor behavior. Tre1 and S1pr1 are thus potent evolutionarily conserved regulators of the elaboration of astrocyte morphological complexity, and ultimately astrocyte control of behavior.

Graphical Abstract

*Lead contacts: freemmar@ohsu.edu, monk@ohsu.edu.

AUTHOR CONTRIBUTIONS

J.C., T.S., K.R.M., and M.R.F. conceived and designed the research. J.C., T.S., Y.K., T.R.J., and A.S. performed the experiments in *Drosophila*, and J.C., D.H., and C.P. performed the experiments in zebrafish. The zebrafish behavioral experiments were performed by K.A.M.N. and F.A. in D.S. lab at NYU, and the fly wind tunnel behavioral experiments were performed by R.J.F. in K.I.N. lab at NYU. J.C., T.S., K.R.M., and M.R.F. wrote the initial draft, and all authors contributed to the final manuscript.

DECLARATION OF INTERESTS

The authors declare no competing interests.

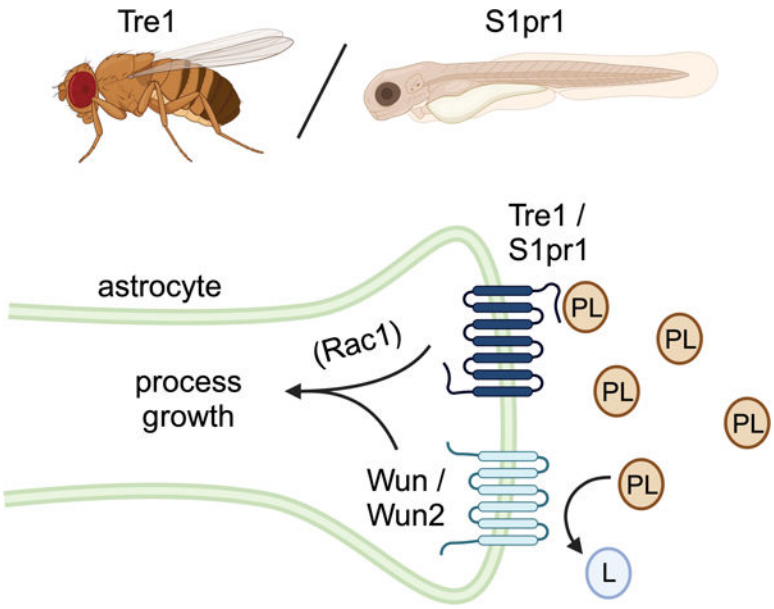

INTRODUCTION

Astrocytes are essential for central nervous system (CNS) development, function, and homeostasis across species. Astrocytes actively participate in synapse formation, pruning, and plasticity during circuit development.[1–4] In myriad ways, astrocytes support neural circuit function by maintaining an optimized environment for neuronal activity.[5–7] Increasing evidence also argues that astrocytes can modulate neural circuit activity and behavior, in some cases by being directly integrated into circuit signaling events.[8,9] A single mammalian astrocyte can interact with thousands of synapses and physiologically bridge them with other CNS cell types. Most astrocyte functions are believed to depend on their profuse membrane specializations and morphological complexity, which act to facilitate widespread signaling across different synapses, the vasculature, and other neighboring CNS cells. Dysregulated astrocyte morphology and function is a hallmark of many neuroinflammatory and neurological diseases,[10–12] but we understand little about the mechanistic basis of astrocyte morphogenesis *in vivo*.

During development astrocytes acquire their elaborate morphology through a stepwise process of vigorous cellular process outgrowth to cover the CNS synaptic space, tiling with adjacent astrocytes, and extension of fine membrane leaflets adjacent to synapses.[6] Heartless/FGF receptor signaling in *Drosophila* acts mainly in a permissive fashion to enable astrocyte process infiltration of the synaptic neuropil, but when FGF ligands are ectopically expressed, astrocyte membranes can be redirected to inappropriate regions of the CNS.[13] Astrocyte tiling in mammals occurs after initial overlap of immature astrocyte territories, followed by the establishment of more precise non-overlapping domains.[14] The boundaries of astrocyte domains are believed to develop through repulsive or competitive interactions with neighboring astrocytes. This notion is supported by the minimal overlap observed between astrocytes in mammals[15], zebrafish[16], and *Drosophila*[13], and the observation that ablation of a subset of *Drosophila* astrocytes during development leads to the expansion of

remaining astrocyte processes into unoccupied regions of the neuropil.[13] In mammals, loss of the cell adhesion molecule HepaCAM reduces astrocyte domain volume, morphological complexity, and astrocyte gap junction coupling,[17] arguing for an important role for HepaCAM in astrocyte morphogenesis. Similarly, the dense network of fine astrocyte leaflets is reduced in animals lacking Neurexin/Neuroligin,[18] which likely serves to coordinate astrocyte-synapse contact sites and synaptogenesis. Astrocyte morphogenesis occurs in parallel with the wiring of neural circuits, and both are intertwined, as astrocyte depletion during development, or the elimination of astrocyte-expressed molecules results in profound abnormalities in neural circuits, including reduced synapse numbers.[3,4,19–24]

The *Drosophila* gene *Tre1* (*Trapped in endoderm 1*) encodes a putative lipid-binding G protein-coupled receptor (GPCR) that promotes the survival and transepithelial migration of germ cells. Maternal *Tre1* RNA is localized to germ cells where it functions cell-autonomously.[25] Wunen (Wun) and Wunen2 (Wun2) are lipid phosphate phosphatases (LPPs), membrane-embedded enzymes that regulate levels of extracellular bioactive lipids such as sphingosine-1-phosphate (S1P) and lysophosphatidic acid.[26] Tre1 is thought to be activated by a phospholipid ligand, which is processed by Wun and/or Wun2 based on the observations that *wun/wun2* mutants partially phenocopy *Tre1* mutants and genetic interaction studies.[27,28] Tre1 belongs to a family of rhodopsin-like GPCRs, which contain two highly conserved domains (NRY and NPxxY motifs), and each domain mediates distinct downstream signaling events.[28] While the phospholipid ligand acting on Tre1 in *Drosophila* germ cell migration is not known, S1P and lipid-binding GPCRs like the S1P receptor 1 (S1pr1) appear to have conserved roles in germ cell migration.[29,30]

In this study, we show lack of Tre1 in astrocytes dramatically reduces the morphological complexity of fine astrocyte processes in *Drosophila*. Tre1 interacts with the small GTPase Rac1, modulating astrocyte process dynamics during outgrowth and organization of the astrocyte cytoskeleton. Wun/Wun2 act in astrocytes to promote astrocyte process outgrowth in a Tre1-dependent fashion. Wun/Wun2 can be repulsive to astrocyte processes when expressed in neurons and can disrupt astrocyte-astrocyte competition when differentially expressed in adjacent astrocytes, arguing for a role for this pathway in establishing individual astrocyte morphological domains. Genetic or pharmacological blockade of S1pr1 signaling in zebrafish similarly perturbs astrocyte growth, and live-imaging of the earliest stages of astrocyte development reveals a key role for S1pr1 in astrocyte process extension/retraction dynamics. Loss of *Tre1*/*s1pr1* in flies or zebrafish leads to behavioral defects in even simple motor-driven behaviors. Our work thus identifies Tre1/S1pr1 and extracellular phospholipids as key regulators of astrocyte morphological development and circuit function from *Drosophila* to vertebrates.

RESULTS

Drosophila Tre1 mutants have smaller astrocytes with reduced morphological complexity

To identify genes enriched in astrocytes, we analyzed existing gene expression databases in *Drosophila*.[31–34] We found that *Tre1* expression is considerably higher in astrocytes than that detected in total brain cells (Figure S1A), and in an unrelated screen for genes required for larval astrocyte engulfment function, we found that expression of a $Tre1^{RNAi}$ construct

in glial cells led to gross defects in astrocyte morphology. To more rigorously test the role of Tre1 in astrocyte morphogenesis, we examined astrocyte morphology in various *Tre1* mutants, in particular the $Tre1^{attP}$ null mutant in which the genomic coding region of *Tre1* is replaced with an *attP* docking site[35] (see also Figure S1B). We labeled adult astrocyte membranes with anti-Gat antibody and presynaptic active zones in the neuropil with anti-Bruchpilot (Brp). In $Tre1^{attP}$ mutants, we found that astrocyte membrane coverage of the antennal lobe (AL) neuropil was dramatically decreased. Astrocytes in $Tre1^{attP}$ mutants did not fully elaborate fine processes to infiltrate olfactory glomeruli, and $Tre1^{attP}$ mutant astrocyte membrane coverage was dramatically reduced compared to controls (Figures 1A, 1C, S1C, and S1D). We found similar phenotypes in $Tre1^{sctt}$ mutants (Figures S1C and S1D), which results from a mis-splicing of the *Tre1* transcript in the coding region.[36] However, we did not observe obvious phenotypes in $Tre1^{\Delta EP5}$ mutants (Figures S1C and S1D), in which the non-coding first exon region of *Tre1* is deleted.[25] The lack of phenotypic effects of the $Tre1^{\Delta EP5}$ mutants is likely due to the use of an alternative *Tre1* transcriptional start in astrocytes that is not affected by the $Tre1^{\Delta EP5}$ mutation (Figure S1B).

We next analyzed astrocyte morphology using the astrocyte-specific driver *alrm-Gal4* to drive *UAS-mCD8-GFP* to label astrocyte membranes. We observed reduced astrocyte infiltration across the entire adult CNS in $Tre1^{attP}$ mutants. In the mushroom body, where wild-type (WT) astrocytes show a slightly lower density of processes compared to other regions of the neuropil,[37] $Tre1^{attP}$ mutants exhibit a near complete absence of astrocyte processes (Figures 1B and 1D). Defects in astrocyte infiltration were already observed during larval stages (Figure S1E) and persisted through adulthood, indicating that Tre1 is required for astrocyte development (Figures S1E and S1F). To determine precisely how individual astrocytes were disrupted in the $Tre1^{attP}$ mutants, we used a FLP-out strategy to generate single-cell astrocyte clones labeled with myristoylated-GFP (myrGFP). We found that, compared to controls, $Tre1^{attP}$ mutant astrocytes occupied a smaller territory in the synaptic neuropil, and the total cell volume was significantly decreased in comparison with WT control astrocytes (Figures 1E and 1F). Taken together, these data indicate that *Tre1* is required for normal astrocyte morphogenesis.

Tre1 acts cell autonomously in astrocytes to regulate membrane growth

To explore the endogenous expression pattern of *Tre1* in the adult brain, we took advantage of the $Tre1^{attP}$ mutation, where an *attP* docking site is inserted at the *Tre1* genomic locus, to generate a $Tre1^{Gal4}$ knock-in allele, in which *Gal4* is co-expressed together with endogenous *Tre1* by a self-cleaving T2A peptide sequence (Figure S1G). $Tre1^{Gal4}$-driven mCD8-mCherry distribution overlapped with Gat-labeled astrocyte membranes in the ALs, and most of the lam-GFP-labeled nuclei were surrounded by anti-Gat staining, indicating they were astrocyte cell bodies (Figure S1H). We next compared $Tre1^{Gal4}$*>mCD8-mCherry* expression with *GMR25H07-LexA>mCD8-GFP*, where astrocytes express the membrane marker mCD8-GFP under *LexA/LexAop* expression system. We observed that $Tre1^{Gal4}$-controlled mCD8-mCherry labeling overlapped with mCD8-GFP-labeled astrocyte membranes throughout the adult brain (Figures 1G and S1I). These data, combined with transcriptomic data, show that *Tre1* expression is highly enriched in *Drosophila* astrocytes.

To determine the cell-autonomy of Tre1 function, we first used the astrocyte *alrm-Gal4* driver to express two independent, non-overlapping *UAS-Tre1* RNAi constructs. By knocking down *Tre1* in astrocytes, the coverage of AL neuropil by astrocyte processes was reduced in both *Tre1* RNAi conditions in contrast to the controls (Figures 1H and S1J). We next generated single-cell RNAi clones using the FLP-out system, where WT astrocytes labeled with mCD8-GFP were adjacent to mCD8-mCherry-labeled clones that were either controls (no RNAi) or expressing $Tre1^{RNAi}$. In control experiments, both the mCD8-GFP- and the mCD8-mCherry-labeled WT astrocytes exhibited dense infiltration of the neuropil, and individual astrocytes (mCD8-mCherry^{+}) occupied unique territories that did not overlap with neighboring cells (Figure 1I). In contrast, when we generated astrocytes expressing $Tre1^{RNAi}$ constructs, the mCD8-mCherry^{+} clones displayed decreased density of processes, with gaps in-between main branches (Figure 1I). We often observed that these gaps were invaded by neighboring mCD8-GFP-labeled WT astrocytes (Figure 1I). Moreover, individual $Tre1^{RNAi}$ astrocytes showed a strongly reduced total volume in comparison with controls (Figures 1J–M). We conclude that *Tre1* is required in astrocytes for normal growth of astrocyte volume and fine leaflets during development, and that WT astrocytes can compensate for gaps in $Tre1^{RNAi}$ astrocytes to ensure full coverage of the neuropil.

To determine whether *Tre1* is required for the maintenance of astrocyte morphology in adults, we first compared expression of *Tre1* at different developmental stages. We found that *Tre1* transcription was largely downregulated in adult astrocytes (Figure S2A). Using a dual-color fluorescent transcriptional timer (TransTimer),[38] we demonstrated that endogenous $Tre1^{Gal4}$-driven transcription activity was active during development but rapidly turned off in the adult (Figure S2B). To directly examine the role of Tre1 in adult astrocytes, we generated a *Tre1* conditional FLP-out line $Tre1^{FRT}$-*Gal4*, in which the *Tre1* genomic locus is flanked by two *FRT* sites that can be induced to delete the *Tre1* gene in a FLPase-dependent manner (Figure S2C). Combining $Tre1^{FRT}$-*Gal4* with the FLP-out system, we induced *Tre1* knockout ($Tre1^{FLP\text{-}out}$) specifically in adult stage astrocytes and found that adult stage $Tre1^{FLP\text{-}out}$ astrocyte clones exhibited densely elaborated processes similar to controls (Figure S2D) and comparable individual astrocyte volumes (Figures S2E and S2F). These data argue that Tre1 is primarily used to establish astrocyte morphology during development, but is dispensable for maintenance of cell architecture in the adult.

Tre1 drives astrocyte growth through its NPIIY motif

In *Drosophila* germ cells, the two conserved NRY and NPIIY motifs of Tre1 are required to guide proper germ cell migration.[28] We generated *UAS-Tre1* rescue constructs with either wild-type *Tre1*, single mutations specific to each domain, or double mutations ($Tre1^{NAY}$, $Tre1^{AAIIY}$, and $Tre1^{NAY,AAIIY}$) [28] (Figure 2A). We assayed for rescue of $Tre1^{attP}$ mutant phenotypes by driving their expression in astrocytes. We found that both wild-type *Tre1* and $Tre1^{NAY}$ transgenes rescued astrocytic coverage of the neuropil in the $Tre1^{attP}$ mutants at levels comparable to that observed in control astrocytes (Figures 2B and S3A). In contrast, neither $Tre1^{AAIIY}$ nor $Tre1^{NAY,AAIIY}$ transgenes could suppress the infiltration defects in the $Tre1^{attP}$ mutant backgrounds (Figures 2B and S3A).

Using the FLP-out strategy, we analyzed single-cell clones in the *Tre1*^{attP} mutant backgrounds. We found that both wild-type *Tre1*- and *Tre1*^{NAY}-expressing astrocyte clones exhibited a WT-like dense infiltration of their processes into the neuropil (Figure 2C), and individual cell volumes were rescued compared to *Tre1*^{attP} mutant clones (Figures 2D and 2E). Interestingly, we also found that individual cell volumes in both wild-type *Tre1*- and *Tre1*^{NAY}-expressing astrocyte clones in *Tre1*^{attP} mutants were significantly larger than WT control astrocyte clones (Figures 2D and 2E), suggesting that Tre1 overexpression can increase astrocyte clone size, which is perhaps enhanced by the presence of neighboring *Tre1*-deficient astrocytes. However, expression of *Tre1*^{AAIIY} or *Tre1*^{NAY,AAIIY} transgenes failed to rescue *Tre1*^{attP} mutant phenotypes (Figures 2C–E). In addition, overexpressing these constructs in astrocytes did not alter astrocyte growth in a WT background, suggesting none of these transgenes dominantly interfere with native Tre1 function (Figures S3B and S3C). Compared to wild-type Tre1 or Tre1^{NAY}, Tre1 proteins with a mutated NPIIY motif (Tre1^{AAIIY} and Tre1^{NAY,AAIIY}) were less distributed into astrocyte processes and showed accumulation in cell bodies, suggesting a role for the NPIIY motif in Tre1 trafficking or turnover (Figure S3D). These results indicate that the Tre1 NPIIY motif, but not the NRY motif, is required for astrocyte morphogenesis, and suggest that the downstream signaling cascades activated by Tre1 in astrocytes are different from those in germ cells where both the NRY and NPIIY motifs drive important signaling events.[28]

Rac1 is essential for nervous system development and well-known for its role in actin cytoskeleton regulation,[39,40] and *in vitro* studies demonstrate that Rac1 can contribute to astrocyte morphological changes.[41] We used three different *Rac1* transgenic lines to explore potential interactions with *Tre1*: *UAS-Rac1.V12* (a constitutively active form of Rac1), *UAS-Rac.N17* (a dominant-negative form of Rac1), and *UAS-Rac1.W* (a wild-type form of Rac1). Expressing constitutively active *Rac1.V12* in astrocytes led to cell death, therefore, we focused our analyses on the other two forms of Rac1. Using the FLP-out system in a WT background, when *Rac1.N17* or *Rac1.W* was misexpressed in single-cell clones labeled with mCD8-mCherry, astrocyte morphology displayed reduced fine process elaboration (Figure 3A), and individual astrocytes showed decreased cell volumes (Figures 3B and 3C). These data suggest that both loss- and gain-of-function in Rac1 signaling are disruptive to astrocyte morphogenesis, and that Rac1 activity needs to be finely tuned for normal astrocyte growth. To test whether *Tre1* genetically interacts with *Rac1*, we next manipulated Rac1 activity in the *Tre1*^{attP} mutant backgrounds. Both *Rac1.N17* and *Rac1.W* expression in astrocytes resulted in an enhancement of defects in astrocyte phenotypes compared to *Tre1*^{attP} mutants alone (Figures 3D and S4A). Individual mCD8-mCherry-labeled astrocytes expressing *Rac1.N17* or *Rac1.W* extended almost no fine membrane processes and their astrocyte volumes were highly reduced in the absence of *Tre1* (Figures 3E–G). Interestingly, we did not observe enhanced phenotypes in the *Tre1*^{attP}/+ heterozygous backgrounds (Figures S4B and S4C), it is therefore unclear whether Rac1 acts downstream or in parallel to Tre1.

Tre1 and Rac1 regulate the astrocyte actin cytoskeleton

We next analyzed astrocyte cytoskeletal organization with cytoskeletal markers Lifeact-GFP.W and chRFP-Tub. We found the actin-rich fine cellular processes and the tubulin-rich major branches were both disrupted in the absence of *Tre1* (Figures S5A and S5B). Using

Lifeact-GFP.W, we analyzed the morphological branching pattern of astrocytes at single-cell resolution using Imaris software (Figures 4A and S5C, S5D; Video S1). While the branch level of individual astrocytes in controls and *Tre1*^{attP} mutants was comparable (Figures 4B and S5E), the branch points and total filament length were significantly reduced in the *Tre1*^{attP} mutants (Figures 4C, 4D and S5F, S5G), and *Tre1*^{attP} mutant astrocytes had an increased percentage of larger filament diameters (Figures 4E and S5H), consistent with the reduced astrocyte membrane coverage in the neuropil we observed (Figure 1A). We found similar results when *Tre1*^{RNAi} was driven in astrocytes (Figures S5I–M), and *Tre1*^{attP} mutant morphological defects could be rescued by re-expression of wild-type *Tre1* in astrocytes, but not by *Tre1*^{NAY,AAIIY} (Figures 4A–E). Tre1 thus plays a cell-autonomous role in regulating cytoskeletal organization in astrocyte fine processes, and loss of *Tre1* leads to a simplified astrocyte morphology with diminished branching and thicker processes.

We next assayed the actin cytoskeletal phenotypes in *Rac1* misexpression experiments. In control WT backgrounds, we found that inhibiting Rac1 activity in astrocytes with Rac1.N17 affected all aspects of cytoskeletal complexity, including decreases in branch level, branch points, and total filament length (Figures S6A–D) and an increase in the larger filament diameter population (Figure S6E). However, astrocytic expression of *Rac1.W* did not influence branch level or the filament diameter distribution, but significantly decreased branch points and total filament length (Figures S6A–E). Moreover, by manipulating Rac1 activity in *Tre1*^{attP} mutants, we observed a strong enhancement of actin cytoskeleton defects (actin branch level, branch points, total filament length, and distribution of filament diameter) by both Rac1.N17 and Rac1.W (Figures 4F–J). Together, these results support the notion that Tre1 and Rac1 both potently regulate astrocyte cytoskeletal organization, but whether they are in the same or parallel genetic pathways remains to be determine.

The lipid-binding GPCR S1pr1 regulates vertebrate astrocyte morphology

GPCRs and extracellular phospholipids control germ cell migration across species.[29,30] We sought to determine whether a lipid-binding GPCR plays a conserved role in vertebrate astrocyte morphogenesis similar to *Drosophila* Tre1. Zebrafish astrocytes are molecularly and functionally similar to their counterparts in *Drosophila* and mammals, and allow for direct visualization of astrocyte morphogenesis throughout development.[16] We first assayed for phenotypes after loss of *Gpr84,* the most closely related vertebrate ortholog of *Drosophila Tre1* by sequence comparison (Figure S7A). We generated a mutation that resulted in 372 base-pair deletion of zebrafish *gpr84* (*gpr84*^{vo87}) using CRISPR/Cas9-mediated genome editing[42,43] (Figure S7B). The *gpr84*^{vo87} mutation generates a truncated Gpr84 protein with two transmembrane domains deleted, likely rendering a non-functional GPCR. In WT zebrafish larval spinal cord at 6 days post-fertilization (dpf), astrocyte cell bodies are adjacent to the midline and emanate fine processes to infiltrate the neuropil, forming a dense meshwork in the lateral regions.[16] Using the astrocyte transgenic line *Tg(slc1a3b:myrGFP-P2A-H2AmCherry),* in which astrocyte membranes are labeled with myrGFP and nuclei are labeled with H2AmCherry, we examined *gpr84*$^{vo87/vo87}$ homozygous mutants in comparison with the control siblings. Astrocytes in *gpr84*$^{vo87/vo87}$ homozygous mutants looked grossly normal at 6 dpf (Figures S7C and S7D), suggesting *gpr84* is not required for astrocyte development in zebrafish.

We next analyzed single-cell RNA-seq and Brain RNA-seq data in zebrafish and mammals[44–47] to identify genes encoding GPCRs, especially lipid-binding GPCRs, that are highly enriched in astrocytes. The gene *s1pr1* (*sphingosine-1-phosphate receptor 1*), which encodes a phospholipid-binding GPCR and belongs to the same GPCR family as *Drosophila* Tre1 (Figure S7A), showed noticeably higher expression in astrocytes. Interestingly, the S1pr1 GPCR has been shown to regulate germ cell migration in the ascidian *B. schlosseri*,[30] similar to the role of Tre1 GPCR in *Drosophila* germ cells.[25] In addition, *in vitro* studies have suggested that S1pr1 can regulate astrocyte morphology in mammals.[48] By whole-mount *in situ* hybridization, we validated that *s1pr1* was expressed in the zebrafish larval brain and spinal cord at 3 dpf (Figure S7E), and we observed expression of *s1pr1* mRNA in myrGFP-labeled astrocytes (Figure S7F). We then used CRISPR/Cas9 to generate two independent *s1pr1* mutant alleles, $s1pr1^{vo88}$ and $s1pr1^{vo89}$, which contain a 270 base-pair or 277 base-pair deletion, respectively, in the coding region of zebrafish *s1pr1* (Figure S7G). Interestingly, we found that astrocyte infiltration to the spinal cord neuropil in the lateral regions was severely disrupted in $s1pr1^{vo88/vo88}$ homozygous mutants in comparison with controls at 6 dpf (Figure 5A). In the *Tg(slc1a3b:myrGFP-P2A-H2AmCherry)* transgenic background, myrGFP-labeled dense astrocyte membranes in the lateral regions of the spinal cord were dramatically diminished in $s1pr1^{vo88/vo88}$ mutants, while the H2AmCherry-labeled nuclei number and position remained largely unaffected (Figures S7H and S7I). These data argue that loss of S1pr1 alters astrocyte morphology, but not cell number. Comparable astrocyte defects were observed in $s1pr1^{vo88/vo89}$ trans-heterozygous mutants (Figures S7K and S7L), and we further validated the phenotypes with the astrocyte marker anti-GS to label zebrafish astrocytes and observed similar results (Figures S7M and S7N).

To analyze astrocyte morphology at the single-cell level, we injected *slc1a3b:myrGFP-P2A-H2AmCherry* DNA constructs into one-celled zygotes to allow for sparse labeling and examined individual astrocyte clones at 6 dpf in the spinal cord. In contrast to control WT astrocytes, which exhibited a ramified morphology with many fine processes, individual $s1pr1^{vo88/vo88}$ mutant astrocytes occupied a smaller spatial domain and had significantly reduced volume (Figures 5B and 5C). Astrocyte development was similarly perturbed throughout the CNS, including in in the forebrain, midbrain, and hindbrain of 6 dpf zebrafish larvae (Figures 5D and S7J), suggesting a requirement for S1pr1 in astrocyte morphogenesis throughout the CNS. Given that Tre1 and S1pr1 are both lipid-binding GPCRs and have been implicated in germ cell migration,[25,30] our results argue that S1pr1 is the functional GPCR analog of Tre1 in vertebrate astrocytes.

S1pr1 functions to balance astrocyte process outgrowth dynamics and is required throughout development

We showed previously that zebrafish astrocytes acquire their complex morphologies between 2 and 4 dpf in the larval spinal cord.[16] We therefore used *slc1a3b:myrGFP* to sparsely label single astrocytes and performed time-lapse confocal microscopy to monitor fine cellular process dynamics at 3 dpf. We observed that astrocyte processes in control astrocytes displayed consistent extension and retraction rates throughout their morphogenesis (Figures 5E and 5F; Video S2). However, $s1pr1^{vo88/vo88}$ mutant astrocyte processes showed both faster extension and retraction speeds in comparison with controls (Figures 5E and 5F;

Video S2), perhaps ultimately leading to excessively dynamic astrocyte processes that prevent establishment of normal contacts. These data demonstrate that astrocyte membrane process dynamics are disrupted in *s1pr1* mutants during astrocyte growth.

Pharmacological S1pr1 modulators, such as FTY720 and Ex26, can be used to acutely block S1pr1 signaling *in vivo*.[49,50] We used these reagents to determine the temporal requirements for S1pr1 signaling in astrocyte morphogenesis. We first treated *Tg(slc1a3b:myrGFP-P2A-H2AmCherry)* transgenic WT zebrafish with 1 μM FTY720 or 1 μM Ex26 from 2 to 4 dpf, stages when astrocytes are rapidly growing in the spinal cord, and found that inhibiting S1pr1 by both FTY720 and Ex26 between 2–4 dpf resulted in disrupted astrocyte morphology by 6 dpf (Figure 5G). Quantification of GFP coverage in astrocyte process-enriched regions revealed that the astrocyte membranes were significantly reduced in FTY720/Ex26-treated larvae compared to DMSO-treated controls (Figure 5H). To determine whether such effects were mediated specifically through S1pr1, we performed similar treatment experiments in the $s1pr1^{vo88/vo88}$ mutant backgrounds between 2–4 dpf, and we found that the astrocyte infiltration defects in $s1pr1^{vo88/vo88}$ mutants were not further exacerbated by either FTY720 or Ex26 (Figures S7O and S7P).

We next asked if S1pr1 inhibition could alter the morphology of more mature astrocytes. We treated zebrafish larvae with FTY720 or Ex26 between 4–6 dpf before imaging. Interestingly, treatment of *Tg(slc1a3b:myrGFP-P2A-H2AmCherry)* transgenic WT larvae also resulted in disruption of astrocytic infiltration of the synaptic neuropil (Figures 5I and 5J). Notably, GFP coverage quantification demonstrated that the astrocyte defects in 4–6 dpf treatment experiments were comparable to that observed in 2–4 dpf treatment experiments (Figures 5H and 5J). Finally, we did not observe exacerbated astrocyte phenotypes for 4–6 dpf FTY720/Ex26 treatment experiments in the $s1pr1^{vo88/vo88}$ mutants, implying the late requirement in astrocyte morphogenesis is also S1pr1-dependent (Figures S7Q and S7R). Based on these results, we conclude that S1pr1 GPCR signaling is required throughout larval astrocyte growth for normal elaboration and maturation of astrocyte morphology *in vivo*.

Tre1/*s1pr1* is required for normal behavioral function in *Drosophila* and zebrafish

We sought to determine whether loss of *Tre1* or *s1pr1* altered neural circuit function. We first assayed odor tracking in *Tre1* mutants in *Drosophila*, which tracks appetitive odors upwind of the odorant source (Figure S8A). We used a wind tunnel apparatus that allowed us to record the position of single animals before, during, and after presentation of the appetitive odor apple cider vinegar (1%)[51] (Figure S8B). Both young (day 5) and old (day 30) $Tre1^{attP}$ mutant flies showed no change in ability to track odor, although we did note a decrease in pre odor ground speed (Figure S8C and S8D). We next tested the climbing activity of *Drosophila* in the absence of *Tre1*, and we found that $Tre1^{attP}$ mutants at 30 dpe exhibited severe climbing defects (Figure 6A). Similar results were detected in astrocyte $Tre1^{RNAi}$ flies at 30 dpe (Figure 6A), and we also observed the climbing defects in astrocyte-specific $Tre1^{KO}$ (*alrm>FLP,Tre1*^{FRT}*-Gal4*) flies (Figure 6B). These results suggest that loss of *Tre1* leads to progressive motor skill deficits in *Drosophila*. Interestingly, when Rac1 activity was manipulated in astrocytes to enhance astrocyte morphological defects in $Tre1^{attP}$ mutants, we began to observe the severe climbing defects in young (3 dpe)

adult flies (Figure 6C), which could indicate that more profound alterations of astrocyte morphology result in more severe behavioral defects.

To determine the functional role of S1pr1 in zebrafish, we assayed for postural behavior and swimming kinematics in WT, *s1pr1*$^{vo89/+}$, and *s1pr1*$^{vo89/vo89}$ larvae using SAMPL[52] (Figure 6D). We found that the number of swim bouts for homozygous mutant fish was significantly reduced compared to controls (Figure 6E), indicating overall swimming deficits. In addition, by analyzing the average posture at peak speed and swim duration, we found that mutant fish tended to have more positive postures which were not corrected during the bout (Figures 6F and 6I), and that mutant fish bouts were on average longer than controls (Figures 6G and 6J), likely indicating challenges in movement initiation or termination. Conversely, we found a reduction in total rotation during the bout (Figures 6H and 6K), which was most prominent during the deceleration phase of the bout. These phenotypes suggest that loss of S1pr1 leads to deficits in sensory processing or integration, as well as impaired mechanisms involved in posture control in zebrafish. Together, these results demonstrate a role for Tre1 and S1pr1 not only in astrocyte morphogenesis, but also animal behavior.

Wunens play opposing roles in astrocytes and neurons to influence astrocyte infiltration

In *Drosophila*, lipid phosphate phosphatases (LPP) Wunen (Wun) and Wunen2 (Wun2) have been shown to function redundantly to hydrolyze phospholipids and to promote the uptake of lipid products into cells.[53,54] Similarly, the vertebrate homologues of Wunen, LPP1-3, can regulate extracellular S1pr1 ligand sphingosine-1-phosphate (S1P) levels and its activity.[55] Loss of *wun*/*wun2* results in germ cell migration defects, similar to the phenotypes observed in *Tre1* mutants, suggesting that Wun/Wun2 may act in the same pathway as Tre1 in *Drosophila.*[25,28] We therefore sought to test the role of Wunens/LPPs in astrocyte morphogenesis.

We first analyzed astrocyte morphology using different *wun* or *wun2* mutants over a deficiency that deletes both *wun/wun2*. Strong *wun*/*wun2* double mutants resulted in pupal lethality, so we analyzed mutant phenotypes in wandering third instar larvae (wL3). Using anti-Gat to label astrocyte membranes in the ventral nerve cord (VNC), we found that loss of single *wunen* genes (*wun*^{23}, *wun*^{9}, or *wun2*^{N14}) did not alter astrocyte morphology grossly in comparison with controls (Figure S9A). However, loss of both *wun* and *wun2* (*wun*^{49},*wun2*^{EX34}) together resulted in relatively mild but clear astrocyte infiltration defects in the VNC (Figure S9A, 8 of 8 animals). This is consistent with previous observations that Wun and Wun2 can act redundantly in other tissues.[53] To determine whether the astrocyte infiltration phenotypes in *wun*/*wun2* mutants were due to a cell-autonomous requirement for Wunen activity, we used the astrocyte driver *alrm-Gal4* to express *wun* or *wun2* specifically in astrocytes. We found that expression of *wun* or *wun2* was sufficient to rescue the infiltration defects to levels similar to controls, while a catalytically dead mutant construct (*wun2*^{H326K}) failed to rescue astrocyte infiltration defects in *wun*^{49},*wun2*^{EX34} mutant backgrounds (Figures 7A and 7B). Overexpression of *wunens* (*wun* or *wun2*) in astrocytes in a control background using the *alrm-Gal4* driver or a stronger astrocyte driver (*GMR25H07-Gal4*) did not alter astrocyte morphology (Figure S9B). In addition, astrocyte expression of mouse *LPP3* (*mLPP3*) in *wun*^{49},*wun2*^{EX34} mutant animals was able

to suppress the infiltration defects (Figures 7A and 7B), demonstrating that mLLP3 can substitute for Wunen activity in *Drosophila* astrocytes.

Unexpectedly, we observed that astrocyte processes extended out of the synaptic neuropil and into the cortex when Wunen activity was restored in astrocytes (Figure 7A). Astrocyte membranes normally remain restricted to the synaptic neuropil unless cortex glia are ablated.[56] To further explore how Wunen regulates astrocyte growth, we employed the Mosaic Analysis with a Repressible Cell Marker (MARCM) approach[57] to analyze $wun^{49}, wun2^{EX34}$ astrocyte mutant clones. Compared to control clones, we found that similar to *Tre1* mutants, individual mutant astrocyte volumes of *wun/wun2* mutant clones were significantly reduced (Figures 7C and 7D). When *wun2* or *wun* was re-expressed in the mutant MARCM clones, the overall astrocyte morphology and cell volumes were significantly rescued (Figures 7C and 7D). Together, these data indicate that Wunen activity is required in astrocytes for normal morphology.

The ectopic astrocyte processes we observed when overexpressing single Wunen in the *wun/wun2* mutants but not in a WT background (Figures 7A and S9B) suggest Wunen might play a role in regulating cell-cell interactions and/or competition with surrounding cells. To explore this further, we first used a pan-neuronal driver *n-syb-Gal4*[58] to misexpress *wun* in all neurons and examined astrocyte infiltration phenotypes. In a WT background, we found that Wunen activity in neurons only moderately altered astrocyte infiltration in the VNC (Figure S9C). In contrast, neuronal expression of *wun* in the $wun^{49}, wun2^{EX34}$ mutant background led to dramatic reduction in astrocyte infiltration of the neuropil, which was not replicated when we used the catalytically dead mutant $wun2^{H326K}$ (Figure S9C). We next used a FLP-out method with *RN2-FLP tub<<Gal4*[59] to manipulate Wunen levels in a subset of mCD8-GFP-labeled neuronal clones in the VNC. Clonal misexpression of *wun* in single neurons in a WT background led to a mild reduction of astrocyte processes within the area of the neuronal clone (Figure S9C). However, we found that expression of *wun* or *wun2* in single neurons resulted in a near complete elimination of astrocytic processes from the domain occupied by the *wunen*-expressing neuron in the *wun/wun2* mutant background (Figures 7E and 7F). This phenotype depended on Wun enzymatic activity and could also be observed, to a lesser extent, with *mLPP3* expression (Figures 7E and 7F). We conclude that neuronal misexpression of Wunen can block the morphological elaboration of surrounding astrocytes, and our data suggests that Wunen activity likely functions very locally in regulating astrocyte growth.

In conclusion, we have shown that Wunen activity is required cell autonomously in astrocytes to promote their proper process elaboration. In addition, we find that Wunen expression in neurons can block astrocyte process outgrowth, most likely by depleting an attractive, growth promoting phospholipid in the environment.

Wunen regulation of astrocyte growth depends on Tre1

We used anti-Gat to label astrocyte membranes to compare the astrocyte morphology in control animals, $wun^{49}, wun2^{EX34}$ mutants, $Tre1^{attP}$ mutants, and the $Tre1^{attP}; wun^{49}, wun2^{EX34}$ triple mutants. As described above, we observed mild astrocyte infiltration defects in $wun^{49}, wun2^{EX34}$ mutants, but stronger infiltration defects in $Tre1^{attP}$

mutants (Figure S10A). When we compared *Tre1*^{attP}; *wun*^{49},*wun2*^{EX34} triple mutants with *Tre1*^{attP} mutants, we found they showed similar astrocyte infiltration defects (Figure S10A). This non-additivity suggests that Tre1 and Wun/Wun2 are in the same genetic pathway in regulation of astrocyte growth. To determine whether Wunen-dependent regulation of astrocyte growth requires Tre1, we used a FLP-out approach to sparsely express *wun2* in myr::tdTomato-labeled astrocyte clones in *wun*^{49},*wun2*^{EX34} mutants or *Tre1*^{attP};*wun*^{49},*wun2*^{EX34} triple mutants. In the *wun*^{49},*wun2*^{EX34} mutant background, *wun2*-expressing astrocyte clones displayed dramatically increased volumes and expanded their territories broadly across the neuropil (Figures 8A–C). This observation further supports the notion that Wunens can potently regulate astrocyte growth. In contrast, in the *Tre1*^{attP}; *wun*^{49},*wun2*^{EX34} triple mutant background, we found that Wunen-mediated astrocyte overgrowth phenotypes were completely suppressed (Figures 8A–C). The expanded process outgrowth we observed in Wun2-overexpressing astrocyte clones in the *wun*^{49},*wun2*^{EX34} mutant background was restricted to the neuropil without prominent projections entering the cortex (Figure 8A), contrary to what might have been expected from global astrocyte expression (Figure 7A). However, clone-adjacent astrocytes (but not those distant from clones) frequently showed prominent membrane projections into the cortex (Figure 8A, arrowheads). The formation of these ectopic astrocyte processes was also suppressed in a *Tre1*^{attP};*wun*^{49},*wun2*^{EX34} triple mutant background, indicating this non-cell autonomous effect of Wun2-overexpressing clones is also dependent on Tre1 activity. This ectopic outgrowth suggests that the cortex can act as a source of attractive phospholipids. To test this idea more directly, we expressed *wun* or *wun2* in astrocytes in a *wun*^{49},*wun2*^{EX34} mutant background. As shown previously (Figure 7A), this leads to pronounced outgrowth of astrocyte processes into the cortex (Figures 8D and 8E). Co-expression of *wun* or *wun2* in astrocytes as well as in cortex glia (*alrm-Gal4* + *GMR54H02-Gal4*^{60}) dramatically suppressed this ectopic outgrowth, suggesting *wun*/*wun2* phospholipase activity in cortex glia is sufficient to deplete the attractive phospholipid in the cortex and prevent ectopic process formation. Together, these data argue strongly that Wunens act in the same signaling pathway as Tre1 to regulate astrocyte morphogenesis, that Tre1 acts downstream of Wunens, and that astrocytes compete with their neighbors for an attractive growth promoting phospholipid that can be inactivated by LPPs.

DISCUSSION

Our work demonstrates the Tre1/S1pr1 GPCR signaling pathway and the lipid phosphate phosphatases (LPPs) Wun and Wun2 are essential for astrocyte morphogenesis in *Drosophila* and zebrafish, and perturbation of these signaling pathways alters animal behavior. Although *s1pr1* is not the closest sequence homolog of *Tre1* in vertebrates, both S1pr1 and Tre1 belong to the rhodopsin-like GPCR family and share the same highly conserved signaling motifs.[61] In addition, these phospholipid-binding GPCRs and S1P have been shown to functionally interact with LPPs in analogous ways during germ cell migration.[28,30,62] Given the strikingly similar astrocyte phenotypes we observed between *Drosophila Tre1* mutants and zebrafish *s1pr1* mutants (Figures 1 and 5) and the fact that they share the same ligand processing enzymes, we propose that Tre1/S1pr1 represent

a functionally conserved phospholipid-mediated GPCR signaling pathway that regulates astrocyte development.

There are important phenotypic differences between the roles of Tre1 and Wun/Wun2 in germ cells versus astrocytes. In germ cells, Tre1 and Wun/Wun2 guide germ cell migration to the gonad and also regulate germ cell survival.[25,28,53,63] In astrocytes, we show these molecules regulate astrocyte process outgrowth and establishment of morphological complexity. We have found no evidence for a role for Tre1/S1pr1 or Wun/Wun2 in astrocyte survival. Our data support the notion that Tre1 might function to balance Rac1 activity through its NPIIY motif to help organize the astrocyte cytoskeleton (Figures 3 and 4). Though we lack a direct biochemical or genetic link, Tre1 activates small GTPases in other contexts, Rac1 has a well-established role in actin cytoskeleton regulation in development and disease,[40,64] and Rac1 is directly involved at the cell membrane to remodel actin dynamics for membrane protrusive behaviors.[65] Live-imaging in zebrafish revealed a role for S1pr1 in the earliest stages of astrocyte process outgrowth, with *s1pr1* mutant astrocytes exhibiting much more dynamic membrane extension/retraction (Figures 5E and 5F). The most parsimonious interpretation of our data is that Tre1/S1pr1 GPCR signaling orchestrates Rac1 activity at the plasma membrane to influence actin-based cellular process protrusions in astrocytes. How could changes in protrusion dynamics lead to a simplified astrocyte morphology? In mouse and zebrafish studies, S1pr1 acts as a negative regulator in endothelial cell growth, by preventing excessive sprouting during angiogenesis and vessel maturation, and the mature vascular network in *s1pr1* mutants is ultimately disorganized with enlarged vessel diameter and reduced vessel number.[66] It is possible that excessive extension/retraction of astrocyte processes in *Tre1* or *s1pr1* mutants similarly disrupts astrocyte morphology, perhaps by altering the ability of astrocytes to form adhesive interactions with surrounding cells, ultimately leading to a simplification of fine processes.

The precise nature of the extracellular phospholipids that activate Tre1 or S1pr1 signaling *in vivo* has been difficult to resolve. To our knowledge, ligands for Tre1 have not been identified. S1P, a ligand for S1pr1 and is believed to also regulate germ cell migration,[30,67] is a candidate for regulating astrocyte growth in vertebrates. The notion that germ cell migration is driven by lipids was first shown in *Drosophila*, where *wun* and *wun2* mutants were found to perturb germ cell migration to the gonad,[27] and other lipid-modifying enzymes have since been shown to play a role in germ cell guidance.[29] We have shown that Wun and Wun2 are potent regulators of astrocyte growth, and this depends on their LPP enzymatic activity. These observations provide strong support for the notion that extracellular phospholipids modulate astrocyte membrane process growth. Where these bioactive phospholipids come from, and how many can regulate astrocyte growth, are open questions, as is the precise nature of their signaling to astrocytes.

How do Tre1 and Wun/Wun2 regulate growth? We found that Wun/Wun2 cell-autonomously facilitate Tre1-dependent growth of astrocytes while neuronal expression of these LPPs can suppress astrocyte outgrowth within the domain of Wun-expressing neurons. The simplest interpretation of our data is that extracellular phospholipids activate Tre1 to positively drive astrocyte growth, and that Wun/Wun2 act locally to process this ligand (Figure S11). We can envision a number possible mechanisms by which Tre1 and Wun/Wun2 signaling might

occur. First, after phospholipid binding to Tre1, the activated receptor promotes astrocyte growth, is internalized, and Wunens dephosphorylate the phospholipid ligand bound to Tre1 to enable receptor recycling to the plasma membrane and continued Tre1 signaling. Interestingly, downregulation of surface S1pr1 receptors is how the therapeutic inhibitor fingolimod is believed to block S1pr1 signaling.[50] Second, Wunens could dephosphorylate phospholipids outside the cell, thereby allowing entry, where lipids are rephosphorylated by sphingosine kinases to activate Tre1 in intracellular vesicles. This is supported by data showing that Wun/Wun2 can promote lipid entry into cells.[53,68] Third, after entry of dephosphorylated lipids into the cell, lipids might be rephosphorylated in a way that makes them bioactive for Tre1, then be transported out of the cell where they can locally activate Tre1 receptors.[68] Ultimately, astrocyte growth would be driven by astrocyte-astrocyte competition for these growth-promoting extracellular phospholipids. According to this model, the ability of neuronal expression to block astrocyte growth would be due to the ability of Wunens to degrade this growth promoting phospholipid, in the domain of the neuron expressing LPPs. Likewise, the lack of overgrowth when Wun or Wun2 are expressed in control animals (versus a *wun, wun2* mutant) would be explained by the ability of neighboring cells to compete for phospholipids.

Tre1 mutant astrocyte phenotypes are more pronounced than those seen in *wun,wun2* double mutants. These observations may indicate that additional LPPs regulate extracellular phospholipid levels involved in astrocyte growth, or other LPP-independent ligands signal through Tre1 in *Drosophila*. Tre1 signaling appears to be sensitive to the relative levels of phospholipids, and Wun/Wun2 seem to regulate the spatial profile of these extracellular lipids. For instance, while clonal Wun or Wun2 overexpression in a WT background did not dramatically alter astrocyte morphology, expression of Wun2 in astrocytes in a *wun,wun2* double mutant background resulted in massive overgrowth of astrocytes in a Tre1-dependent fashion. Here, the Wun2-expressing cell has a competitive advantage over its neighbors due to its ability to facilitate Tre1 signaling cell autonomously and the inability of the neighboring cells to inactivate the phospholipid in their territory.

How astrocytes determine their territories in relation to other astrocytes is poorly understood.[13,69,70] Our data supports a model in which Tre1/S1pr1 and Wunen/LPPs are well poised to control competitive interactions between neighboring astrocytes, analogous to their roles in germ cell development.[53] Tre1/S1pr1 acts as the receptor for a bioactive phospholipid to promote astrocyte process outgrowth and elaboration, and Wunen/LPPs cell-autonomously facilitate Tre1/S1pr1 signaling while also degrading free phospholipids to deprive neighboring cells from this growth promoting factor. We propose that the Tre1/S1pr1 and Wunen/LPP system, together with other signaling systems like FGF-signaling[13,16,71] and cell contact dependent interactions[18,72,73], is a major contributor to astrocyte-astrocyte territorial competition and tiling.[14,15] Unexpectedly, in Wunen/LPP rescue experiments we observed prominent projections of astrocytes into the cortex (Figure 7A), suggesting that Wunen function is not restricted to astrocyte-astrocyte interactions but that astrocytes are also competing with cortex glia that ensheath the neuronal cell bodies.[56] This is not a strictly cell-autonomous function of Wun2 overexpression: clonal rescues show that while the Wun2 expressing cells show substantial overgrowth in the neuropil, it is the non-expressing immediately neighboring astrocytes that grow ectopic processes into the

cortex (Figure 8A). This is likely due to the efficient depletion of active phospholipid in the neuropil by the Wun2-expressing clone, with residual phospholipid in the cortex that can still activate Tre1-dependent process outgrowth. This interpretation is further supported by the fact that the ectopic astrocyte processes observed in the CNS cell cortex in rescue experiments (Figure 7A) can be efficiently suppressed by co-expression of *wun*/*wun2* in cortex glia (Figures 8D and 8E), presumably by depleting the attractive phospholipid in the region of the cell cortex.

Our experiments to pharmacologically inhibit S1pr1 indicate that S1pr1 activity is continuously required to guide astrocyte morphogenesis during development at the larval stages in zebrafish (Figure 5). Tre1 appears to be dispensable to maintain normal astrocyte morphology in flies, but it remains to be determined how astrocytes in the adult CNS respond to S1pr1 blockade. This is an important question in the context of human health as the S1pr1 modulator FTY720 (Fingolimod) is a bioactive compound that has been used in humans to treat multiple sclerosis (MS).[74,75] FTY720 is thought to act through peripheral immune-based mechanisms to reduce egress of lymphocytes from lymph nodes to prevent T cell-elicited neuroinflammation to the CNS. FTY720 can also cross the blood-brain barrier to target astrocytes to ameliorate astrogliosis-associated neurodegeneration in MS.[76] Given our findings for a role of S1pr1 in zebrafish astrocyte development, and the continued expression of *s1pr1* in mature zebrafish astrocytes, it remains an interesting question as to whether FTY720 could alter adult astrocyte morphology.

STAR METHODS

RESOURCE AVAILABILITY

Lead contact—Further information and requests for resources and reagents should be directed to and will be fulfilled by the lead contacts, Marc R. Freeman (freemmar@ohsu.edu) and Kelly R. Monk (monk@ohsu.edu).

Materials availability—Plasmids and transgenic lines generated in this study are available upon request.

Data and code availability

- All data reported in this paper will be shared by the lead contact upon request.
- This paper does not report original code.
- Any additional information required to reanalyze the data reported in this paper is available from the lead contact upon request.

EXPERIMENTAL MODEL AND STUDY PARTICIPANT DETAILS

***Drosophila* strains—**Flies (*Drosophila melanogaster*) were kept on standard cornmeal molasses agar with a 12hr/12hr light cycle at 25°C. The following lines were used: w^{1118}, $Tre1^{attP}$[35], $Tre1^{\Delta EP5}$ and $Tre1^{sctt}$ gift from R. Lehmann, Whitehead Institute, Cambridge, MA United States[28], *Df(2R) BSC408*[77], $wun2^{N14}$, *Df(2R)w45-19g*[63], wun^{23}, wun^{9}[53], wun^{49} $wun2^{EX34}$[78], *UAS-wun*[27], *UAS-wun2-GFP*[79], and *UAS-*

wun2^{H326K} [54], *UAS-mLPP3* [79], *alrm-Gal4* [80], *UAS-mCD8-GFP* [57], *Tre1*^{Gal4} (this study), *Tre1*^{FRT}*-Gal4* (this study), *UAS-TransTimer* (Bloomington, 93411), *hsFLPD5.fco* [81], *alrm>nlsLexAfl>Gal4co* (this study), *alrm>QF>Gal4* (this study), *10XUAS-IVS-myrGFP* [82], *10XUAS-IVS-myr::tdTomato* (Bloomington 32221), *UAS-Lifeact-GFP.W* (Bloomington, 57326), *UAS-chRFP-Tub* (Bloomington, 25773), *UAS-mCD8-mCherry* [13], *UAS-lam-GFP* [83], *GMR25H07-Gal4* (Bloomington, 49145), *GMR54H02-Gal4* (Bloomington, 45784), *GMR25H07-LexA* (Bloomington, 52711), *13xLexAop2-mCD8-GFP* [82], *UAS-Tre1*^{KK102307} RNAi (VDRC, v108952), *UAS-Tre1*^{HMS00599} RNAi (Bloomington, 33718), *5xUAS-Tre1*, *5xUAS-Tre1*^{NAY}, *5xUAS-Tre1*^{AAIIY}, and *5xUAS-Tre1*^{NAY,AAIIY} (this study), *UAS-Rac1.N17* and *UAS-Rac1.W* [40], *RN2-FLP tub-Gal4 UAS-mCD8-GFP* [59], *n-syb-Gal4* [58].

Zebrafish husbandry and transgenic lines—All zebrafish studies were performed in compliance with institutional ethical regulations for animal testing and research at Oregon Health & Science University (OHSU). Experiments were approved by the Institutional Animal Care and Use Committee of OHSU. Zebrafish were maintained at 28°C and fed with a combination of rotifer suspension, brine shrimp, and dry food (Gemma 75, 150, 300). Zebrafish embryos and larvae were raised at 28.5°C in petri dishes with embryo medium, and phenylthiourea (PTU, 0.004% final concentration) was used to reduce pigmentation after 24 hpf for live imaging experiments. The following lines were used in this study: AB wild-type, *gpr84*^{vo87}, *s1pr1*^{vo88}, and *s1pr1*^{vo89} (this study), and *Tg(slc1a3b:myrGFP-P2A-H2AmCherry)*[16].

METHOD DETAILS

Generation of *Tre1* endogenous Gal4 reporter flies—To generate the *Tre1* endogenous Gal4 reporter line (*Tre1*^{Gal4}), we first modified the *pBsk-attB-13687-Gal4* (gift from Y. Rao, Peking University, Beijing China)[35] to replace the *13687* sequence with NheI-AgeI-NotI restriction enzyme sites. We subsequently PCR amplified the genomic DNA sequence spanning the coding region of *Tre1* to be inserted using NheI and AgeI to generate *pBsk-attB-Tre1-Gal4*. The construct was sequence verified by Sanger sequencing (Genewiz) and used for transgenesis (Bestgene), and the resulting stable stock was further crossed with a Cre line (Bloomington, 1092) to excise the exogenous markers (*w*$^{+}$ and *3xP3-RFP*) via the flanking *LoxP* sites (Figure S1). Primer sequences are described in Table S1.

Generation of *Tre1* conditional FLP-out flies—To generate the *Tre1* conditional knockout line (*Tre1*^{FRT}*-Gal4*), we modified *pBsk-attB-Tre1-Gal4* construct using a Gibson assembly cloning kit (NEB) to insert a *FRT* site at the 5' region of *Tre1* locus and hsp70 termination sequence with a *FRT* site at the 3' region of *Tre1* locus to generate *pBsk-attB-FRT-Tre1-FRT-Gal4* (*pBsk-attB>Tre1>Gal4*). Similar to the generation of *Tre1*^{Gal4} line, this construct was sequence verified by Sanger sequencing (Genewiz) and used for transgenesis (Bestgene), and the resulting stable stock was further crossed with a Cre line (Bloomington, 1092) to excise the exogenous markers (*w*$^{+}$ and *3xP3-RFP*) via the flanking *LoxP* sites. The two *FRT* sites flanking endogenous *Tre1* locus therefore can be used to induce conditional knockout of Tre1 using a *FLP* line.

Generation of *UAS-Tre1* expressing transgenes—We PCR amplified the sequences from constructs of *nos$_p$-tre1+ flag*, *nos$_p$-tre1 NRY− flag*, *nos$_p$-tre1 NPIIY− flag*, and *nos$_p$-tre1 NRY−NPIIY− flag* gift from R. Lehmann, Whitehead Institute, Cambridge, MA United States; [28] and subcloned into the *pattB-5xUAS* vector using XhoI and XbaI digestion sites. All the constructs were sequence verified by Sanger sequencing (Genewiz) and used for *attP2* landing site-specific integration on the 3rd chromosome. Primer sequences are described in Table S1.

Generation of *alrm*>QF>Gal4 (*alrm*-QNUG)—The *alrm*-QNUG (**Q**F **N**o **U**TR **G**al4co) was generated similar to a previously published version of this flip-out construct (Stork et al. 2014) but, lacks the dedicated 3' Hsp70 terminator for the QF cassette but retains a SV40 terminator for the Gal4co. In short, QF was amplified from *pCaSpeR-EFAN-FRT-QF-HSP70-FRT-Gal4co* using the primers *QF NotI for* and *SpeI FRT QF noUTR rev* and cloned into *pCaSpeR-EFAN-Gal4co* via NotI/SpeI sites to form *pCaSpeR-EFAN FRT-QF-noUTR-FRT-Gal4co*. The *alrm* promotor was amplified from genomic DNA with the primers *Alrm FseI for* and *Alrm AscI rev* and inserted into *pCaSpeR-EFAN FRT-QF-noUTR-FRT-Gal4co* via FseI/AscI sites to form *pCaSpeR-EFAN-alrm-QNUG*.

Generation of *gcm*-FLP and *ftz*-FLP—A DNA fragment containing a DSCP basal promoter, Syn21 5'UTR (Pfeiffer et al., 2012) FLPD5 (Nern et al., 2011) coding sequence and a P10 3'UTR (Pfeiffer et al., 2012) were codon optimized and synthesized by Genescript and delivered in a *puc57* vector. Subsequently this fragment was transferred into a modified *pCaSpeR* vector *pCaSpeR-EFAN* (Stork et al. 2014) via NotI/XhoI sites to form *pCaSpeR-EFAN-FLP*.

The *gcm* promoter region of 9kb (Ragone et al., 2002) was amplified from the genomic P[acman] BAC clone CH322-71L23 (Venken et al., 2009) in two 4.5 kb fragments with the primers *gcm 9–4.5 Gibson for*, *gcm 9–4.5 rev*, *gcm 4.5–0 for* and *gcm 4.5–0 Gibson rev* that were subsequently cloned into an AscI/ NotI digested *pCaSpeR-EFAN-FLP* using Gibson assembly (Gibson et al. 2009). For the *ftz*-FLP construct, a 127 bp fragment of the *fushi tarazu* Promoter/5'UTR (Jacobs et al. 1989) was PCR amplified from genomic DNA with the primers *ftz for NotI* and *ftz rev BamHI* and cloned into *pCaSpeR-EFAN-FLP* via NotI/BamHI restriction removing the DSCP basal promoter from the final construct. The *alrm*>nlsLexAfl>Gal4co, *alrm*>QF>Gal4, *gcm*-FLP, and *ftz*-FLP transgenes were generated by P-element mediated transgenesis at Bestgene.

Generation of mutants in zebrafish—We used CRISPR/Cas9 method to generate genetic mutants in zebrafish. The web tool of CHOPCHOP [84] was used to select target sites, and individual *sgRNAs* were synthesized using MEGAshortscript T7 Transcription kit (Thermo Fisher). *sgRNAs* were mixed with Cas9 Nuclease (Integrated DNA Technologies) to a final concentration of 50–100 ng/μL each *sgRNA* and 1 μg/μL of Cas9 protein, and injected into one-celled zygotes at the volume of 1–2 nL. Progeny of injected F_0 generation were screened for the presence of inherited indels resulting in frameshifts or truncations, and these F_1 progenies were used to establish stable mutant lines. All *sgRNA* sequences and genotyping primers are listed in Table S1.

Translating Ribosome Affinity Purification Sequencing

***Drosophila* strains:** To generate flies in which ribosomes were tagged in astrocytes, flies with elaV-Gal80 (Yang et al., 2009; doi: 10.1016/j.neuron.2008.12.021) were crossed with alrm-Gal4, UAS-EGFP-L10a (Huang et al., 2013; doi: 10.1371/journal.pbio.1001703). Pupae were collected at 48–72hr after puparium formation (APF), and adults collected at 1–3 days post-eclosion (dpe), 10–12dpe and 50–60dpe. Two hundred flies were pooled for each sample, and 3–5 samples were evaluated at each time point.

Sample preparation: Pupal samples were aligned in a petri dish pretreated with RNase ZAP. A razor blade was used to isolate approximately the anterior third of the pupae, which contains the brain and ventral nerve cord. This tissue was then transferred into an RNase free Eppendorf tube and kept on ice until 50 pupae were collected, no longer than 20min. Samples were then stored at −80°C. Adult samples were prepared by freezing flies at −80°C in 15mL conical tubes. These tubes were then vortexed vigorously to remove the heads. The contents of these tubes were then poured onto a white notecard placed over dry ice. Heads were collected using a paintbrush and 200 heads per tube were collected. Heads were stored at −80°C until use.

Lysate preparation: Samples were homogenized in lysis buffer (20mM HEPES KOH pH7.4, 5mM $MgCl_2$, 150mM KCl, protease inhibitor, with 0.5mM DTT, 100μg/mL cyclohexamide, 50μg/mL emetine, 10μl/mL SUPERase-In RNAse inhibitor and 10μl/mL RNase OUT ribonuclease inhibitor added right before use). 250μl buffer was added to each tube of 50 pupal samples and each tube of 200 adult heads. Samples were then placed on ice and homogenized for 20–30s using a motorized hand-held homogenizer with pestles fitted to 1.5mL Eppendorf tube (Biomasher II, Kimble). After homogenization, lysis buffer was added to adult head samples to bring them up to 1mL. Samples were spun down at 2060g to remove nuclei. Supernatants from four pupal samples were pooled into a new 1.5mL tube, so that 1mL lysate from a total of 200 pupae were combined into each sample, and additional lysis buffer if needed to bring up to a total volume of 1mL. For adult samples, 1mL supernatant was transferred into a new tube. To each sample, 111μl NP-40 was added and was mixed gently by inversion. Then, 123μl DHPC was added, mixed gently by inversion and incubated on ice for 5min. Samples were centrifuged at 16,100g at 4°C for 15min.

Bead preparation: 375μl of Protein G Dynalbeads were prepared for each sample. Beads were washed 3 times for 5min with shaking in a 0.15M KCl wash buffer (20mM HEPES-KOH pH7.4, 150mM KCl, 5mM $MgCl_2$, 1% NP-40, with 0.5mM DTT, 100μg/mL cyclohexamide and 50μg/mL emetine added immediately before use) and were pelleted using a magnetic stand. Stock solutions of cyclohexamide were prepared in MeOH at a concentration of 100mg/mL and emetine prepared in EtOH at a concentration of 50mg/mL. After the third wash, beads were resuspended in 0.15M KCl and GFP antibodies (50μg of each of HTZGFP-19C8 and HTZGFP-19F7) up to a total volume of 375μl per sample. Beads were incubated at RT for 2 hours with end-over-end rotation. Unbound antibody was removed by washing 3 times for 5min in the 0.15M KCl wash buffer.

Pull-down: For each sample, 1mL supernatant was transferred to the washed, GFP-bound beads. Beads were resuspended in sample lysates and incubated at 4°C with end over end rotation for 30min. Beads were then washed 3 times for 5min at 4°C in 0.35M KCl wash buffer (20mM HEPES-KOH pH7.4, 350mM KCl, 5mM $MgCl_2$, 1%NP-40, with 0.5mM DTT, 100μg/mL cyclohexamide and 50μg/mL emetine added immediately before use). Samples were then placed on ice for up to 20min.

RNA recovery: Buffer was removed and samples were resuspended in RLT buffer (Qiagen RNA minielute kit) with BMe added just before use. Tubes was mixed by inversion to resuspend the beads and placed on ice. RNA isolation was performed according to the instructions provided in the kit. RNA was eluted by adding 10μl of water to the membrane, spinning for 1min, and then adding another 10μl of water and repeating the spin step.

RNA sequencing and analysis: RNA quality and quantity was assessed using a NanoDrop and an Agilent 2100 Bioanalyzer and RNA 60000 PicoChip, run with the eukaryotic total RNA program. Concentrations ranged from 3.1–3.3 ng/μl as measured by NanoDrop and 476–480 pg/μl as measured with the Agilent RNA 6000 Pico Assay, with 260/280 ratios averaging 1.8 and 260/230 ratios averaging 0.03. RIN values ranged from 5.9–8.0. cDNAs were prepared with the SmartSeq Ultra Low Input kit (Takara). The cDNAs were fragmented with an S220 sonicator and sequencing libraries prepared using aTruSeq Stranded ribosomal reduction protocol (Illumina). Libraries were profiled with a TapeStation (Agilent) and quantified using an NGS Quantification Kit (Kapa BioSystems/Roche) on a StepOnePlus Real Time PCR workstation (Thermo/ABI). Libraries were sequenced on a NovaSeq6000 (Illumina) using 2x100 cycle sequencing with paired end reads on a NovaSeq S4 flow cell with 50 million templates / sample. Fastq files were assembled using bcl2fastq (Illumina). Read quality was assessed using the FastQC pipeline. Alignment was performed using the *Drosophila melanogaster* BDGP6 reference genome.

Immunohistochemistry

***Drosophila* staining:** Dissection and immunostaining of adult fly brains were performed according to the FlyLight Protocols (https://www.janelia.org/project-team/flylight/protocols). Adult fly brains were dissected in cold 1xPBS (phosphate buffered saline, Invitrogen), and fixed in 2% paraformaldehyde (PFA, Electron Microscopy Sciences) in 1xPBS for 55 minutes at room temperature. Fixed brains were washed four times with PBSTr (5% Triton X-100 in 1xPBS) while nutating for 20–25 minutes per wash at room temperature. Blocking was performed in 5% normal goat serum (Jackson ImmunoResearch) in PBSTr (0.5% Triton X-100 in 1xPBS) for 1.5–2 hours at room temperature on a nutator. Primary and secondary antibodies were diluted in PBSTr (0.5% Triton X-100) and incubated with samples at 4°C for 48–72 hours. Washes after the primary and secondary antibody incubations were carried out at room temperature with PBSTr for 4 x 25 minutes. Stained samples were mounted with VECASHIELD antifade mounting medium (Vector Laboratories) and stored at 4°C until imaging. Larval CNS dissections were performed in 1xPBS, and fixed in 4% FA/1xPBS for 25 minutes at room temperature. Larval CNS dissections were washed and blocked in PBST-BSA (0.2%Trition X-100 in 1XPBS, with 1% Bovine Serum Albumin). Primary antibodies were diluted in PBST without any blocking

agent and were incubated at 4°C for about 48h. Subsequently the samples were washed with PBST 5x for a total time of 1h. Secondary antibodies were diluted in PBST-BSA and incubated at 4°C for about 48 hours, washed with PBST 5x for a total time of 1 hour and mounted in CFM-1 with antifade (Citifluor) and stored at 4°C until analysis on a confocal microscope. Primary antibodies were used as follows: rabbit anti-Gat (1:2500, [13]), chicken anti-GFP (1:1000, ab13970, abcam), rat anti-mCherry (1:1000, M11217, Thermo Fisher), rabbit anti-RFP (1:1000, 600-401-379, Rockland Inc.), mouse anti-nc82 (1:25, Developmental Studies Hybridoma Bank), anti-Pros (MR1A, 1:150, Developmental Studies Hybridoma Bank), mouse anti-FLAG (1:1000, F1804, Sigma-Aldrich). Secondary antibodies used include: Donkey secondary antibodies conjugated to Alexa Fluor 488/647 or Rhodamine Red-X (1:250, Jackson ImmunoResearch), horse anti-mouse DyLight 649 (1:250, DI-2649, Vector Laboratories), and goat anti-rabbit DyLight 649 (1:250, DI-1649, Vector Laboratories).

Zebrafish staining: Zebrafish larvae were fixed in 4% PFA/1xPBS at 4°C overnight and then incubated with 150 mM Tris-HCl, pH 9.0 at 70°C for 15 minutes for antigen retrieval [85]. Fixed larvae were subsequently permeabilized with 100% acetone at −20°C for 20 minutes, and mouse anti-GS (1:1 prediluted, Sigma-Aldrich) antibody staining was performed as described previously [16]. Stained samples were mounted in VECASHIELD antifade mounting medium (Vector Laboratories) for imaging.

Whole-mount *in situ* hybridization in zebrafish—To examine the expression patterns of *s1pr1* in zebrafish, we PCR amplified the coding region of *s1pr1* with a T7 promoter sequence in the reverse primer from 2–3 dpf larval stage wild-type cDNA. The anti-sense RNA probes of *s1pr1* were synthesized using Digoxigenin RNA Labeling Kit (Sigma-Aldrich), and whole-mount *in situ* hybridization was performed as previously described [86]. 3 dpf zebrafish were fixed in 4% PFA/1xPBS at 4°C overnight and dehydrated with 100% methanol at −20°C for at least 48 hours prior to the following steps. Dehydrated samples were rehydrated through a series of methanol/PBS washes for 10 minutes each at room temperature with an additional 3 x 10 minutes PBSTw (0.1% Tween-20) and treated with proteinase K (1:1000, Bioline) for 20 minutes to increase permeabilization. Samples were then postfixed with 4% PFA/1xPBS for 20 minutes at room temperature, and rinsed 5 x 5 minutes with PBSTw. Pre-hybridization was performed at 65°C in hybridization buffer (50% formamide, 5x SSC, 50 μg/mL heparin, 500 μg/mL transfer RNA, 100 mM citric acid, and 0.1% Tween-20 in dH2O) for at least 4 hours. After prehybridization, samples were incubated with digoxigenin-labeled *s1pr1* RNA probe in hybridization buffer at 65°C overnight. Anti-digoxigenin-AP antibody was used at 1:2000 and followed by alkaline phosphatase staining assay. Stained samples were kept in 80% glycerol at 4°C until imaging.

Whole-mount immuno-coupled hybridization chain reaction (WICHCR)—WICHCR for *s1pr1* mRNA and GFP protein on 6 dpf *Tg(slc1a3b:myrGFP-P2A-H2AmCherry)* transgenic fish was performed by following an established STAR Protocol [87]. In short, 6 dpf larvae were fixed in 4% PFA, dehydrated in MeOH, and rehydrated in PBST (0.1% Tween-20 in 1x PBS). Larvae were permeabilized with 100% acetone at −20°C and digested with 2 mg/mL proteinase K for 1 hour at room temperature (RT). After

post-fixation with 4% PFA, larval heads and tails were clipped off for efficient penetration of the probes and antibodies. *s1pr1*-B1 HCR probe set was designed against NM_131691.3 (Molecular Instruments) along with other HCR reagents and B1-Alexa Fluor 647. For IF, anti-GFP antibody (Aves) was used at 1:250 and anti-chicken Alexa Fluor 546 was used at 1:500. Larvae were cleared in serial glycerol solutions and mounted in 0.8% agarose for confocal imaging.

Sparse labeling using FLP-out and MARCM in *Drosophila*—To sparsely label adult fly astrocytes with single-cell clones using the FLP-out system, we collected *hsFLPD5.fco;alrm>nlsLexAfl>Gal4co,13xLexAop2-mCD8-GFP,UAS-mCD8-mCherry* or *hsFLPD5.fco;alrm>nlsLexAfl>Gal4co,UAS-mCD8-mCherry;UAS-Lifeact-GFP.W* pupae with the corresponding genotypes (*UAS-RNAi*, wild-type, or *Tre1* mutant backgrounds) at 0–16 h APF and heat shocked at 37°C for 10 minutes at 32–48 h APF. Under these conditions, the FLP-out clones will have the *FRT*-flanking *nlsLexAfl (>nlsLexAfl>*) cassette excised and begin to express *Gal4/UAS*-driven transgenes in the astrocytes. The heat shocked pupae were then incubated at 25°C until eclosion. Adult brain dissections were performed at 1–3 dpe, and subjected to immunostaining described as above before imaging. Similarly larval FLP-out clones were generated using an *alrm*>QF>Gal4co, *UAS-mCD8-mCherry, ftz-FLP stock.* The activity of *ftz*-FLP leads to early and relatively sparse labeling of Gal4 expressing astrocyte (and to some degree ensheathing glia) clones.

To induce adult stage *Tre1* FLP-out deletion, $Tre1^{FRT}$*-Gal4* female flies were crossed with *hsFLPD5.fco;alrm>nlsLexAfl>Gal4co,13xLexAop2-mCD8-GFP,UAS-mCD8-mCherry* male in a wild-type or $Tre1^{attP}$ mutant background. Corresponding progenies were collected and incubated at 25°C, FLPase activity was induced by heat-shock at 37°C for 10–15 minutes at 1–3 dpe. In this manner, a copy of FRT-flanking endogenous *Tre1* (*>Tre1>*) was deleted specifically at the adult stage. The heat shocked adult flies were then kept at 25°C for 14 days before brain dissections and subsequent immunostaining/imaging procedures.

MARCM clones were generated by crossing *FRTG13 tub-Gal80 repo-Gal80; alrm-Gal4, UAS-CD8-Cherry, gcm-FLP* to *FRTG13* controls or *FRT42B* wun^{49} $wun2^{Ex34}$ or *FRT42B* wun^{49} $wun2^{Ex34}$ combined with UAS-*wun* or UAS-*wun2*-GFP on the third chromosome. Note that *FRT42B* and *FRTG13* are the same FRT insertion but are named differently in different research contexts. This *gcm-FLP* MARCM system generates routinely 80–90% of L3 larvae with VNC astrocyte clones.

Zebrafish microinjections and mosaic labeling—To label zebrafish astrocytes at the single-cell level, we injected 20–30 pg of *slc1a3b:myrGFP-P2A-H2AmCherry* DNA constructs into one-celled zygotes and allowed the embryos to develop at 28.5°C until desired developmental stages for imaging. We assayed individual spinal cord astrocyte volumes at 6 dpf, and we chose to live-image the dynamics of astrocyte elaboration at 3 dpf when astrocytes are actively growing in the spinal cord [16].

Image acquisition and processing—Imaging of fixed fly CNS or zebrafish larvae was performed using Zeiss LSM 880 and LSM 980 with Airyscan 2 confocal microscopes, or

an Innovative Imaging Innovations (3i) spinning-disk confocal microscope equipped with a Yokogawa CSX-X1 scan head. For high-resolution astrocyte imaging, confocal z stacks were acquired using the optimal z-interval and around 0.05–0.09 μm/pixel resolution with either a 40x/1.2 Plan-Apochromat Imm Corr or a 40x/1.3 Plan-Apochromat oil objective. Images were Airyscan processed, images tiles stiched when necessary, and converted into IMARIS format for 3D analysis.

Zebrafish *in vivo* imaging—To live-image astrocyte morphogenesis in zebrafish, 3 dpf larvae were anesthetized with 0.16 mg/mL of Tricaine in embryo medium and mounted in 1.0% low-melting agarose laterally on a cover slip with extra embryo medium containing Tricaine sealed inside a vacuum grease ring to prevent evaporation. Time-lapse imaging on *slc1a3b:myrGFP-P2A-H2AmCherry*+ astrocyte clones were performed in 40–50 μm z-stack with 0.5 μm z-interval every 10 minutes for 1.5–2 hours. Owing to the z-stack sometimes being insufficient to include an entire astrocyte clone, the z-stack was adjusted to focus on the astrocyte cellular processes where the dynamic astrocytic outgrowths were occurring. Acquired time-lapse images were Airyscan processed, and followed by Bleach correction and 3D drift correction using Fiji (ImageJ) software before analysis.

Chemical treatments—FTY720 and Ex26 (Tocris Bioscience) were dissolved in DMSO to a stock concentration of 100 mM. To treat zebrafish, the stock solution was diluted to a final concentration of 1 μM with embryo medium with 0.1% DMSO. The *Tg(slc1a3b:myrGFP-P2A-H2AmCherry)* fish were incubated with the diluted solution starting at 2 dpf or 4 dpf for 48 hours, rinsed several times with embryo medium, and incubated with fresh embryo medium until imaging. Control fish were treated with 0.1% DMSO in embryo medium for same period of time. 6 dpf larvae were then mounted dorsally on a cover slip in 1.2% low-melting agarose for imaging.

Drosophila behavioral experiments

Wind Tunnel Behavioral Assay: For behavioral experiments the $Tre1^{attP}$ line was backcrossed to w^{1118} (Bloomington, 5905) for seven generations. Wind tunnel behavioral assays were performed in the miniature wind tunnel apparatus as previously described[51] (Design can be found at https://github.com/nagellab/AlvarezSalvado_ElementaryTransformations). Flies were collected and were placed in time shifted boxes 2–7 days before experiment. Flies were starved 16–24 hours before the assay. Flies were run at subjective Zeitgeber time 1–6. Flies were anesthetized on ice and then placed in a shallow acrylic arena. Flies were allowed to recover for ~ 5 minutes before beginning experiments. Each arena had a constant laminar airflow of ~12 cm/s and flies were tracked using IR LEDs and a camera. Trials were 70 s long and were randomly interleaved between trials with and without odor. Odor, when present, was 1% apple cider vinegar beginning at 30 s and lasting for 10 s. At least 80 trials were performed for each fly.

Fly positions were tracked in real time using a custom LabView Code (https://github.com/nagellab/AlvarezSalvado_ElementaryTransformations), analysis was performed in Matlab and figure plotting and statistics were performed in GraphPad Prism.

Climbing assay: Fly climbing experiments were performed as previously described[88]. Briefly, 10–20 flies were anesthetized using CO_2 at 0–1 dpe and collected to incubate at 25°C for at least 24 hours before testing. At 3 dpe or 30 dpe, flies were transferred to an empty vial and given ~30 minutes to habituate. The experiments were conducted by tapping the vial to examine for negative geotaxis activity. Each fly was analyzed at 20 second after tapping to determine whether passing the target line (50% vial height). A percentage was calculated for each group (10–20 flies). This percentage for each group is represented as a single date point, and several groups (see corresponding figure legends) were tested in each assay.

Zebrafish behavior experiments—Zebrafish behavior experiments were performed to measure the posture and swimming kinematics of unconstrained freely swimming fish[52]. Behavior data were analyzed using custom-written MATLAB software. Bouts were extracted from the raw data using a 5mm/s threshold for bout detection and various parameters were saved in MATLAB files. Only bouts during the circadian day were analyzed. Behavior was recorded in constant darkness. If an experimental repeat (=48h recording of 4 fish in one arena) contained less than 250 bouts it was excluded. If an experimental repeat contained more than 3500 bouts, 3500 bouts were randomly selected for analysis. For the analysis, swim bouts were aligned at peak speed (defined as time 0) and only bouts with peak speed >5mm/s were included in the analysis. The analyzed parameters were defined as following: posture: refers to the pitch angle of the fish at peak speed; angular velocity: angular velocity is the change in pitch angle over time; total rotation: area under the angular velocity curve between −250ms and 250ms; duration of bout: time during bout where the fish is moving faster than 1mm/s. As single experiments do not contain enough data, the data are combined for different experiments and the error is calculated using resampling technique jackknifing (one experiment is left out and the median of the remaining ones is calculated). To exclude potential background effects only parameters where WT and heterozygous were comparable were analyzed. Given that the morphology of heterozygous fish was unchanged we concluded that changes between WT and heterozygous are due to background differences.

QUANTIFICATION AND STATISTICAL ANALYSIS

To quantify individual astrocyte volumes and densities, we used the Surface module in IMARIS 9 (Bitplane). For astrocyte cellular structure analyses, we used the Filament module in IMARIS 9 with default settings in the software. Ectopic process outgrowth into the cortex was counted in orthogonal 3D projections of 100 μm of neuropil along the anterior-posterior axis generated in IMARIS. Quantification of astrocyte process coverage area was performed by thresholding the green pixel area using Fiji in a 10 μm x 10 μm square region at a similar z-plane image in the AL or manually selected region-of-interest (ROI) in the MB lobe area, two data points were generated from the independent AL or MB in each animal. To quantify the extension and retraction speed of zebrafish astrocyte individual processes, we manually curated the tracking results from frame to frame, and averaged the mean speed for each individually-tracked objects. Quantification of drug treatment experiments on *Tg(slc1a3b:myrGFP-P2A-H2AmCherry)* zebrafish astrocytes were performed by thresholding the green pixel area from 4 independent regions in the

astrocyte processes infiltrated areas in the CNS, and similar z-plane images were taken from individual fish. For fly wind tunnel behavioral analysis, we compared the mean values of each motor parameter at 10 s before odor, 10 s during odor and 10 s after odor. To quantify zebrafish behavioral data, a Kruskal-Wallis test with multiple comparisons was used. All parameters are shown as median and IQR for the zebrafish behavioral data. All statistical analyses were carried out using GraphPad Prism 8/9; statistical details, p values, and numbers of analyzed samples are indicated in the figure legends. Individual cell data points were used to analyze the statistics for individual astrocyte volumes and cytoskeleton structure. Groups were compared using unpaired t test and one-way ANOVA multiple-comparison with Tukey's test unless specified in the figure legends.

Supplementary Material

Refer to Web version on PubMed Central for supplementary material.

ACKNOWLEDGMENTS

We would like to thank Dr. Y. Rao, Dr. R. Lehmann, Dr. A. Renault, and Dr. T. Awasaki for kindly providing us plasmids and flies, the Bloomington Stock Center and the Vienna Drosophila RNAi Center for fly stocks, and the Developmental Studies Hybridoma Bank, created by the NICHD of the NIH and maintained at The University of Iowa, Department of Biology, Iowa City, IA 52242 for select monoclonal antibodies. We thank A. Forbes and T. Perry for excellent zebrafish care, and colleagues from the Freeman and Monk labs for helpful comments and discussion on the manuscript. This work was supported by R37NS053538 to M.R.F., R21NS115437 to K.R.M., R01NS124146 to M.R.F. and K.R.M., F32NS117647 to T.R.J., and F32NS129591 to D.H. from NIH, and Damon Runyon Fellowship 2329-18 to Y.K..

REFERENCES

1. Lee JH, Kim JY, Noh S, Lee H, Lee SY, Mun JY, Park H, and Chung WS (2021). Astrocytes phagocytose adult hippocampal synapses for circuit homeostasis. Nature 590, 612–617. 10.1038/s41586-020-03060-3. [PubMed: 33361813]
2. Chung WS, Clarke LE, Wang GX, Stafford BK, Sher A, Chakraborty C, Joung J, Foo LC, Thompson A, Chen C, et al. (2013). Astrocytes mediate synapse elimination through MEGF10 and MERTK pathways. Nature 504, 394–400. 10.1038/nature12776. [PubMed: 24270812]
3. Allen NJ, Bennett ML, Foo LC, Wang GX, Chakraborty C, Smith SJ, and Barres BA (2012). Astrocyte glypicans 4 and 6 promote formation of excitatory synapses via GluA1 AMPA receptors. Nature 486, 410–414. 10.1038/nature11059. [PubMed: 22722203]
4. Christopherson KS, Ullian EM, Stokes CC, Mullowney CE, Hell JW, Agah A, Lawler J, Mosher DF, Bornstein P, and Barres BA (2005). Thrombospondins are astrocyte-secreted proteins that promote CNS synaptogenesis. Cell 120, 421–433. 10.1016/j.cell.2004.12.020. [PubMed: 15707899]
5. Freeman MR, and Doherty J (2006). Glial cell biology in Drosophila and vertebrates. Trends Neurosci 29, 82–90. 10.1016/j.tins.2005.12.002. [PubMed: 16377000]
6. Allen NJ, and Barres BA (2009). Neuroscience: Glia - more than just brain glue. Nature 457, 675–677. 10.1038/457675a. [PubMed: 19194443]
7. Khakh BS, and Sofroniew MV (2015). Diversity of astrocyte functions and phenotypes in neural circuits. Nat Neurosci 18, 942–952. 10.1038/nn.4043. [PubMed: 26108722]
8. Bazargani N, and Attwell D (2016). Astrocyte calcium signaling: the third wave. Nat Neurosci 19, 182–189. 10.1038/nn.4201. [PubMed: 26814587]
9. Nagai J, Yu X, Papouin T, Cheong E, Freeman MR, Monk KR, Hastings MH, Haydon PG, Rowitch D, Shaham S, and Khakh BS (2021). Behaviorally consequential astrocytic regulation of neural circuits. Neuron 109, 576–596. 10.1016/j.neuron.2020.12.008. [PubMed: 33385325]
10. Burda JE, and Sofroniew MV (2014). Reactive gliosis and the multicellular response to CNS damage and disease. Neuron 81, 229–248. 10.1016/j.neuron.2013.12.034. [PubMed: 24462092]

11. Han RT, Kim RD, Molofsky AV, and Liddelow SA (2021). Astrocyte-immune cell interactions in physiology and pathology. Immunity 54, 211–224. 10.1016/j.immuni.2021.01.013. [PubMed: 33567261]
12. Molofsky AV, Krencik R, Ullian EM, Tsai HH, Deneen B, Richardson WD, Barres BA, and Rowitch DH (2012). Astrocytes and disease: a neurodevelopmental perspective. Genes Dev 26, 891–907. 10.1101/gad.188326.112. [PubMed: 22549954]
13. Stork T, Sheehan A, Tasdemir-Yilmaz OE, and Freeman MR (2014). Neuron-glia interactions through the Heartless FGF receptor signaling pathway mediate morphogenesis of Drosophila astrocytes. Neuron 83, 388–403. 10.1016/j.neuron.2014.06.026. [PubMed: 25033182]
14. Bushong EA, Martone ME, and Ellisman MH (2004). Maturation of astrocyte morphology and the establishment of astrocyte domains during postnatal hippocampal development. Int J Dev Neurosci 22, 73–86. 10.1016/j.ijdevneu.2003.12.008. [PubMed: 15036382]
15. Bushong EA, Martone ME, Jones YZ, and Ellisman MH (2002). Protoplasmic astrocytes in CA1 stratum radiatum occupy separate anatomical domains. J Neurosci 22, 183–192. [PubMed: 11756501]
16. Chen J, Poskanzer KE, Freeman MR, and Monk KR (2020). Live-imaging of astrocyte morphogenesis and function in zebrafish neural circuits. Nat Neurosci 23, 1297–1306. 10.1038/s41593-020-0703-x. [PubMed: 32895565]
17. Baldwin KT, Tan CX, Strader ST, Jiang C, Savage JT, Elorza-Vidal X, Contreras X, Rulicke T, Hippenmeyer S, Estevez R, et al. (2021). HepaCAM controls astrocyte self-organization and coupling. Neuron 10.1016/j.neuron.2021.05.025.
18. Stogsdill JA, Ramirez J, Liu D, Kim YH, Baldwin KT, Enustun E, Ejikeme T, Ji RR, and Eroglu C (2017). Astrocytic neuroligins control astrocyte morphogenesis and synaptogenesis. Nature 551, 192–197. 10.1038/nature24638. [PubMed: 29120426]
19. Delaney CL, Brenner M, and Messing A (1996). Conditional ablation of cerebellar astrocytes in postnatal transgenic mice. J Neurosci 16, 6908–6918. [PubMed: 8824329]
20. Tsai HH, Li H, Fuentealba LC, Molofsky AV, Taveira-Marques R, Zhuang H, Tenney A, Murnen AT, Fancy SP, Merkle F, et al. (2012). Regional astrocyte allocation regulates CNS synaptogenesis and repair. Science 337, 358–362. 10.1126/science.1222381. [PubMed: 22745251]
21. Eroglu C, Allen NJ, Susman MW, O'Rourke NA, Park CY, Ozkan E, Chakraborty C, Mulinyawe SB, Annis DS, Huberman AD, et al. (2009). Gabapentin receptor alpha2delta-1 is a neuronal thrombospondin receptor responsible for excitatory CNS synaptogenesis. Cell 139, 380–392. 10.1016/j.cell.2009.09.025. [PubMed: 19818485]
22. Kucukdereli H, Allen NJ, Lee AT, Feng A, Ozlu MI, Conatser LM, Chakraborty C, Workman G, Weaver M, Sage EH, et al. (2011). Control of excitatory CNS synaptogenesis by astrocyte-secreted proteins Hevin and SPARC. Proceedings of the National Academy of Sciences of the United States of America 108, E440–449. 10.1073/pnas.1104977108. [PubMed: 21788491]
23. Muthukumar AK, Stork T, and Freeman MR (2014). Activity-dependent regulation of astrocyte GAT levels during synaptogenesis. Nat Neurosci 17, 1340–1350. 10.1038/nn.3791. [PubMed: 25151265]
24. Ackerman SD, Perez-Catalan NA, Freeman MR, and Doe CQ (2021). Astrocytes close a motor circuit critical period. Nature 592, 414–420. 10.1038/s41586-021-03441-2. [PubMed: 33828296]
25. Kunwar PS, Starz-Gaiano M, Bainton RJ, Heberlein U, and Lehmann R (2003). Tre1, a G protein-coupled receptor, directs transepithelial migration of Drosophila germ cells. PLoS biology 1, E80. 10.1371/journal.pbio.0000080. [PubMed: 14691551]
26. Morris AJ, Smyth SS, Salous AK, and Renault AD (2013). Lipid Phosphate Phosphatases: Recent Progress and Assay Methods. In Lysophospholipid Receptors, pp. 229–263. 10.1002/9781118531426.ch12.
27. Zhang N, Zhang J, Purcell KJ, Cheng Y, and Howard K (1997). The Drosophila protein Wunen repels migrating germ cells. Nature 385, 64–67. 10.1038/385064a0. [PubMed: 8985246]
28. LeBlanc MG, and Lehmann R (2017). Domain-specific control of germ cell polarity and migration by multifunction Tre1 GPCR. The Journal of cell biology 216, 2945–2958. 10.1083/jcb.201612053. [PubMed: 28687666]

29. Richardson BE, and Lehmann R (2010). Mechanisms guiding primordial germ cell migration: strategies from different organisms. Nature reviews. Molecular cell biology 11, 37–49. 10.1038/nrm2815. [PubMed: 20027186]

30. Kassmer SH, Rodriguez D, Langenbacher AD, Bui C, and De Tomaso AW (2015). Migration of germline progenitor cells is directed by sphingosine-1-phosphate signalling in a basal chordate. Nature communications 6, 8565. 10.1038/ncomms9565.

31. Ng FS, Sengupta S, Huang Y, Yu AM, You S, Roberts MA, Iyer LK, Yang Y, and Jackson FR (2016). TRAP-seq Profiling and RNAi-Based Genetic Screens Identify Conserved Glial Genes Required for Adult Drosophila Behavior. Front Mol Neurosci 9, 146. 10.3389/fnmol.2016.00146. [PubMed: 28066175]

32. Huang Y, Ng FS, and Jackson FR (2015). Comparison of larval and adult Drosophila astrocytes reveals stage-specific gene expression profiles. G3 5, 551–558. 10.1534/g3.114.016162. [PubMed: 25653313]

33. Davie K, Janssens J, Koldere D, De Waegeneer M, Pech U, Kreft L, Aibar S, Makhzami S, Christiaens V, Bravo Gonzalez-Blas C, et al. (2018). A Single-Cell Transcriptome Atlas of the Aging Drosophila Brain. Cell 174, 982–998 e920. 10.1016/j.cell.2018.05.057. [PubMed: 29909982]

34. Brunet Avalos C, Maier GL, Bruggmann R, and Sprecher SG (2019). Single cell transcriptome atlas of the Drosophila larval brain. Elife 8. 10.7554/eLife.50354.

35. Deng B, Li Q, Liu X, Cao Y, Li B, Qian Y, Xu R, Mao R, Zhou E, Zhang W, et al. (2019). Chemoconnectomics: Mapping Chemical Transmission in Drosophila. Neuron 101, 876–893 e874. 10.1016/j.neuron.2019.01.045. [PubMed: 30799021]

36. Kamps AR, Pruitt MM, Herriges JC, and Coffman CR (2010). An evolutionarily conserved arginine is essential for Tre1 G protein-coupled receptor function during germ cell migration in Drosophila melanogaster. PLoS One 5, e11839. 10.1371/journal.pone.0011839. [PubMed: 20676220]

37. Kremer MC, Jung C, Batelli S, Rubin GM, and Gaul U (2017). The glia of the adult Drosophila nervous system. Glia 65, 606–638. 10.1002/glia.23115. [PubMed: 28133822]

38. He L, Binari R, Huang J, Falo-Sanjuan J, and Perrimon N (2019). In vivo study of gene expression with an enhanced dual-color fluorescent transcriptional timer. Elife 8. 10.7554/eLife.46181.

39. Ng J, Nardine T, Harms M, Tzu J, Goldstein A, Sun Y, Dietzl G, Dickson BJ, and Luo L (2002). Rac GTPases control axon growth, guidance and branching. Nature 416, 442–447. 10.1038/416442a. [PubMed: 11919635]

40. Luo L, Liao YJ, Jan LY, and Jan YN (1994). Distinct morphogenetic functions of similar small GTPases: Drosophila Drac1 is involved in axonal outgrowth and myoblast fusion. Genes Dev 8, 1787–1802. 10.1101/gad.8.15.1787. [PubMed: 7958857]

41. Racchetti G, D'Alessandro R, and Meldolesi J (2012). Astrocyte stellation, a process dependent on Rac1 is sustained by the regulated exocytosis of enlargeosomes. Glia 60, 465–475. 10.1002/glia.22280. [PubMed: 22144092]

42. Jinek M, Chylinski K, Fonfara I, Hauer M, Doudna JA, and Charpentier E (2012). A programmable dual-RNA-guided DNA endonuclease in adaptive bacterial immunity. Science 337, 816–821. 10.1126/science.1225829. [PubMed: 22745249]

43. Jao LE, Wente SR, and Chen W (2013). Efficient multiplex biallelic zebrafish genome editing using a CRISPR nuclease system. Proceedings of the National Academy of Sciences of the United States of America 110, 13904–13909. 10.1073/pnas.1308335110. [PubMed: 23918387]

44. Farnsworth DR, Saunders LM, and Miller AC (2020). A single-cell transcriptome atlas for zebrafish development. Developmental biology 459, 100–108. 10.1016/j.ydbio.2019.11.008. [PubMed: 31782996]

45. Spanjaard B, Hu B, Mitic N, Olivares-Chauvet P, Janjuha S, Ninov N, and Junker JP (2018). Simultaneous lineage tracing and cell-type identification using CRISPR-Cas9-induced genetic scars. Nat Biotechnol 36, 469–473. 10.1038/nbt.4124. [PubMed: 29644996]

46. Zhang Y, Sloan SA, Clarke LE, Caneda C, Plaza CA, Blumenthal PD, Vogel H, Steinberg GK, Edwards MS, Li G, et al. (2016). Purification and Characterization of Progenitor and Mature

Human Astrocytes Reveals Transcriptional and Functional Differences with Mouse. Neuron 89, 37–53. 10.1016/j.neuron.2015.11.013. [PubMed: 26687838]

47. Zhang Y, Chen K, Sloan SA, Bennett ML, Scholze AR, O'Keeffe S, Phatnani HP, Guarnieri P, Caneda C, Ruderisch N, et al. (2014). An RNA-sequencing transcriptome and splicing database of glia, neurons, and vascular cells of the cerebral cortex. J Neurosci 34, 11929–11947. 10.1523/JNEUROSCI.1860-14.2014. [PubMed: 25186741]
48. Singh SK, Kordula T, and Spiegel S (2021). Neuronal contact upregulates astrocytic sphingosine-1-phosphate receptor 1 to coordinate astrocyte-neuron cross communication. Glia 10.1002/glia.24135.
49. Cahalan SM, Gonzalez-Cabrera PJ, Nguyen N, Guerrero M, Cisar EA, Leaf NB, Brown SJ, Roberts E, and Rosen H (2013). Sphingosine 1-phosphate receptor 1 (S1P(1)) upregulation and amelioration of experimental autoimmune encephalomyelitis by an S1P(1) antagonist. Mol Pharmacol 83, 316–321. 10.1124/mol.112.082958. [PubMed: 23204443]
50. Matloubian M, Lo CG, Cinamon G, Lesneski MJ, Xu Y, Brinkmann V, Allende ML, Proia RL, and Cyster JG (2004). Lymphocyte egress from thymus and peripheral lymphoid organs is dependent on S1P receptor 1. Nature 427, 355–360. 10.1038/nature02284. [PubMed: 14737169]
51. Alvarez-Salvado E, Licata AM, Connor EG, McHugh MK, King BM, Stavropoulos N, Victor JD, Crimaldi JP, and Nagel KI (2018). Elementary sensory-motor transformations underlying olfactory navigation in walking fruit-flies. Elife 7. 10.7554/eLife.37815.
52. Zhu Y, Auer F, Gelnaw H, Davis SN, Hamling KR, May CE, Ahamed H, Ringstad N, Nagel KI, and Schoppik D (2023). Scalable Apparatus to Measure Posture and Locomotion (SAMPL): a high-throughput solution to study unconstrained vertical behavior in small animals. bioRxiv 10.1101/2023.01.07.523102.
53. Renault AD, Sigal YJ, Morris AJ, and Lehmann R (2004). Soma-germ line competition for lipid phosphate uptake regulates germ cell migration and survival. Science 305, 1963–1966. 10.1126/science.1102421. [PubMed: 15331773]
54. Starz-Gaiano M, Cho NK, Forbes A, and Lehmann R (2001). Spatially restricted activity of a Drosophila lipid phosphatase guides migrating germ cells. Development 128, 983–991. 10.1242/dev.128.6.983. [PubMed: 11222152]
55. Tang X, Benesch MG, and Brindley DN (2015). Lipid phosphate phosphatases and their roles in mammalian physiology and pathology. J Lipid Res 56, 2048–2060. 10.1194/jlr.R058362. [PubMed: 25814022]
56. Coutinho-Budd JC, Sheehan AE, and Freeman MR (2017). The secreted neurotrophin Spatzle 3 promotes glial morphogenesis and supports neuronal survival and function. Genes Dev 31, 2023–2038. 10.1101/gad.305888.117. [PubMed: 29138279]
57. Lee T, and Luo L (1999). Mosaic analysis with a repressible cell marker for studies of gene function in neuronal morphogenesis. Neuron 22, 451–461. 10.1016/s0896-6273(00)80701-1. [PubMed: 10197526]
58. Rao SS, Stewart BA, Rivlin PK, Vilinsky I, Watson BO, Lang C, Boulianne G, Salpeter MM, and Deitcher DL (2001). Two distinct effects on neurotransmission in a temperature-sensitive SNAP-25 mutant. EMBO J 20, 6761–6771. 10.1093/emboj/20.23.6761. [PubMed: 11726512]
59. Ou Y, Chwalla B, Landgraf M, and van Meyel DJ (2008). Identification of genes influencing dendrite morphogenesis in developing peripheral sensory and central motor neurons. Neural Dev 3, 16. 10.1186/1749-8104-3-16. [PubMed: 18616799]
60. Jenett A, Rubin GM, Ngo TT, Shepherd D, Murphy C, Dionne H, Pfeiffer BD, Cavallaro A, Hall D, Jeter J, et al. (2012). A GAL4-driver line resource for Drosophila neurobiology. Cell Rep 2, 991–1001. 10.1016/j.celrep.2012.09.011. [PubMed: 23063364]
61. Zhou Q, Yang D, Wu M, Guo Y, Guo W, Zhong L, Cai X, Dai A, Jang W, Shakhnovich EI, et al. (2019). Common activation mechanism of class A GPCRs. Elife 8. 10.7554/eLife.50279.
62. Paksa A, Bandemer J, Hoeckendorf B, Razin N, Tarbashevich K, Minina S, Meyen D, Biundo A, Leidel SA, Peyrieras N, et al. (2016). Repulsive cues combined with physical barriers and cell-cell adhesion determine progenitor cell positioning during organogenesis. Nat Commun 7, 11288. 10.1038/ncomms11288. [PubMed: 27088892]

63. Hanyu-Nakamura K, Kobayashi S, and Nakamura A (2004). Germ cell-autonomous Wunen2 is required for germline development in Drosophila embryos. Development 131, 4545–4553. 10.1242/dev.01321. [PubMed: 15342479]
64. Liang J, Oyang L, Rao S, Han Y, Luo X, Yi P, Lin J, Xia L, Hu J, Tan S, et al. (2021). Rac1, A Potential Target for Tumor Therapy. Front Oncol 11, 674426. 10.3389/fonc.2021.674426. [PubMed: 34079763]
65. Ridley AJ, Paterson HF, Johnston CL, Diekmann D, and Hall A (1992). The small GTP-binding protein rac regulates growth factor-induced membrane ruffling. Cell 70, 401–410. 10.1016/0092-8674(92)90164-8. [PubMed: 1643658]
66. Ben Shoham A, Malkinson G, Krief S, Shwartz Y, Ely Y, Ferrara N, Yaniv K, and Zelzer E (2012). S1P1 inhibits sprouting angiogenesis during vascular development. Development 139, 3859–3869. 10.1242/dev.078550. [PubMed: 22951644]
67. Mendelson K, Evans T, and Hla T (2014). Sphingosine 1-phosphate signalling. Development 141, 5–9. 10.1242/dev.094805. [PubMed: 24346695]
68. Kono M, Hoachlander-Hobby LE, Majumder S, Schwartz R, Byrnes C, Zhu H, and Proia RL (2022). Identification of two lipid phosphatases that regulate sphingosine-1-phosphate cellular uptake and recycling. J Lipid Res 63, 100225. 10.1016/j.jlr.2022.100225. [PubMed: 35568252]
69. DeSantis DF, and Smith CJ (2021). Tetris in the Nervous System: What Principles of Neuronal Tiling Can Tell Us About How Glia Play the Game. Front Cell Neurosci 15, 734938. 10.3389/fncel.2021.734938. [PubMed: 34512272]
70. Torres-Ceja B, and Olsen ML (2022). A closer look at astrocyte morphology: Development, heterogeneity, and plasticity at astrocyte leaflets. Curr Opin Neurobiol 74, 102550. 10.1016/j.conb.2022.102550. [PubMed: 35544965]
71. Kang K, Lee SW, Han JE, Choi JW, and Song MR (2014). The complex morphology of reactive astrocytes controlled by fibroblast growth factor signaling. Glia 62, 1328–1344. 10.1002/glia.22684. [PubMed: 24796693]
72. Baldwin KT, Tan CX, Strader ST, Jiang C, Savage JT, Elorza-Vidal X, Contreras X, Rulicke T, Hippenmeyer S, Estevez R, et al. (2021). HepaCAM controls astrocyte self-organization and coupling. Neuron 109, 2427–2442 e2410. 10.1016/j.neuron.2021.05.025. [PubMed: 34171291]
73. Takano T, Wallace JT, Baldwin KT, Purkey AM, Uezu A, Courtland JL, Soderblom EJ, Shimogori T, Maness PF, Eroglu C, and Soderling SH (2020). Chemico-genetic discovery of astrocytic control of inhibition in vivo. Nature 588, 296–302. 10.1038/s41586-020-2926-0. [PubMed: 33177716]
74. Brinkmann V, Billich A, Baumruker T, Heining P, Schmouder R, Francis G, Aradhye S, and Burtin P (2010). Fingolimod (FTY720): discovery and development of an oral drug to treat multiple sclerosis. Nat Rev Drug Discov 9, 883–897. 10.1038/nrd3248. [PubMed: 21031003]
75. Kappos L, Antel J, Comi G, Montalban X, O'Connor P, Polman CH, Haas T, Korn AA, Karlsson G, Radue EW, and Group FDS (2006). Oral fingolimod (FTY720) for relapsing multiple sclerosis. N Engl J Med 355, 1124–1140. 10.1056/NEJMoa052643. [PubMed: 16971719]
76. Choi JW, Gardell SE, Herr DR, Rivera R, Lee CW, Noguchi K, Teo ST, Yung YC, Lu M, Kennedy G, and Chun J (2011). FTY720 (fingolimod) efficacy in an animal model of multiple sclerosis requires astrocyte sphingosine 1-phosphate receptor 1 (S1P1) modulation. Proceedings of the National Academy of Sciences of the United States of America 108, 751–756. 10.1073/pnas.1014154108. [PubMed: 21177428]
77. Cook RK, Christensen SJ, Deal JA, Coburn RA, Deal ME, Gresens JM, Kaufman TC, and Cook KR (2012). The generation of chromosomal deletions to provide extensive coverage and subdivision of the Drosophila melanogaster genome. Genome Biol 13, R21. 10.1186/gb-2012-13-3-r21. [PubMed: 22445104]
78. Renault AD, Kunwar PS, and Lehmann R (2010). Lipid phosphate phosphatase activity regulates dispersal and bilateral sorting of embryonic germ cells in Drosophila. Development 137, 1815–1823. 10.1242/dev.046110. [PubMed: 20431117]
79. Ile KE, Tripathy R, Goldfinger V, and Renault AD (2012). Wunen, a Drosophila lipid phosphate phosphatase, is required for septate junction-mediated barrier function. Development 139, 2535–2546. 10.1242/dev.077289. [PubMed: 22675212]

80. Doherty J, Logan MA, Tasdemir OE, and Freeman MR (2009). Ensheathing glia function as phagocytes in the adult Drosophila brain. J Neurosci 29, 4768–4781. 10.1523/JNEUROSCI.5951-08.2009. [PubMed: 19369546]

81. Nern A, Pfeiffer BD, Svoboda K, and Rubin GM (2011). Multiple new site-specific recombinases for use in manipulating animal genomes. Proceedings of the National Academy of Sciences of the United States of America 108, 14198–14203. 10.1073/pnas.1111704108. [PubMed: 21831835]

82. Pfeiffer BD, Ngo TT, Hibbard KL, Murphy C, Jenett A, Truman JW, and Rubin GM (2010). Refinement of tools for targeted gene expression in Drosophila. Genetics 186, 735–755. 10.1534/genetics.110.119917. [PubMed: 20697123]

83. Aza-Blanc P, Lin HY, Ruiz i Altaba A, and Kornberg TB (2000). Expression of the vertebrate Gli proteins in Drosophila reveals a distribution of activator and repressor activities. Development 127, 4293–4301. 10.1242/dev.127.19.4293. [PubMed: 10976059]

84. Labun K, Montague TG, Krause M, Torres Cleuren YN, Tjeldnes H, and Valen E (2019). CHOPCHOP v3: expanding the CRISPR web toolbox beyond genome editing. Nucleic Acids Res 47, W171–W174. 10.1093/nar/gkz365. [PubMed: 31106371]

85. Inoue D, and Wittbrodt J (2011). One for all--a highly efficient and versatile method for fluorescent immunostaining in fish embryos. PLoS One 6, e19713. 10.1371/journal.pone.0019713. [PubMed: 21603650]

86. Cunningham RL, and Monk KR (2018). Whole Mount In Situ Hybridization and Immunohistochemistry for Zebrafish Larvae. Methods in molecular biology 1739, 371–384. 10.1007/978-1-4939-7649-2_25. [PubMed: 29546721]

87. Ibarra-Garcia-Padilla R, Howard A.G.A.t., Singleton EW, and Uribe RA (2021). A protocol for whole-mount immuno-coupled hybridization chain reaction (WICHCR) in zebrafish embryos and larvae. STAR Protoc 2, 100709. 10.1016/j.xpro.2021.100709. [PubMed: 34401776]

88. Madabattula ST, Strautman JC, Bysice AM, O'Sullivan JA, Androschuk A, Rosenfelt C, Doucet K, Rouleau G, and Bolduc F (2015). Quantitative Analysis of Climbing Defects in a Drosophila Model of Neurodegenerative Disorders. J Vis Exp, e52741. 10.3791/52741. [PubMed: 26132637]

89. Yang CH, Rumpf S, Xiang Y, Gordon MD, Song W, Jan LY, and Jan YN (2009). Control of the postmating behavioral switch in Drosophila females by internal sensory neurons. Neuron 61, 519–526. 10.1016/j.neuron.2008.12.021. [PubMed: 19249273]

90. Huang Y, Ainsley JA, Reijmers LG, and Jackson FR (2013). Translational profiling of clock cells reveals circadianly synchronized protein synthesis. PLoS biology 11, e1001703. 10.1371/journal.pbio.1001703. [PubMed: 24348200]

- The GPCR Tre1 and LPPs Wun/Wun2 promote astrocyte process outgrowth in *Drosophila*
- Astrocytes compete for a growth-promoting phospholipid in the CNS
- Phospholipid phosphatases Wun/Wun2 act locally to regulate local PL levels and process outgrowth through Tre1
- Vertebrate S1pr1 regulates astrocyte growth early, through modulation of process dynamics

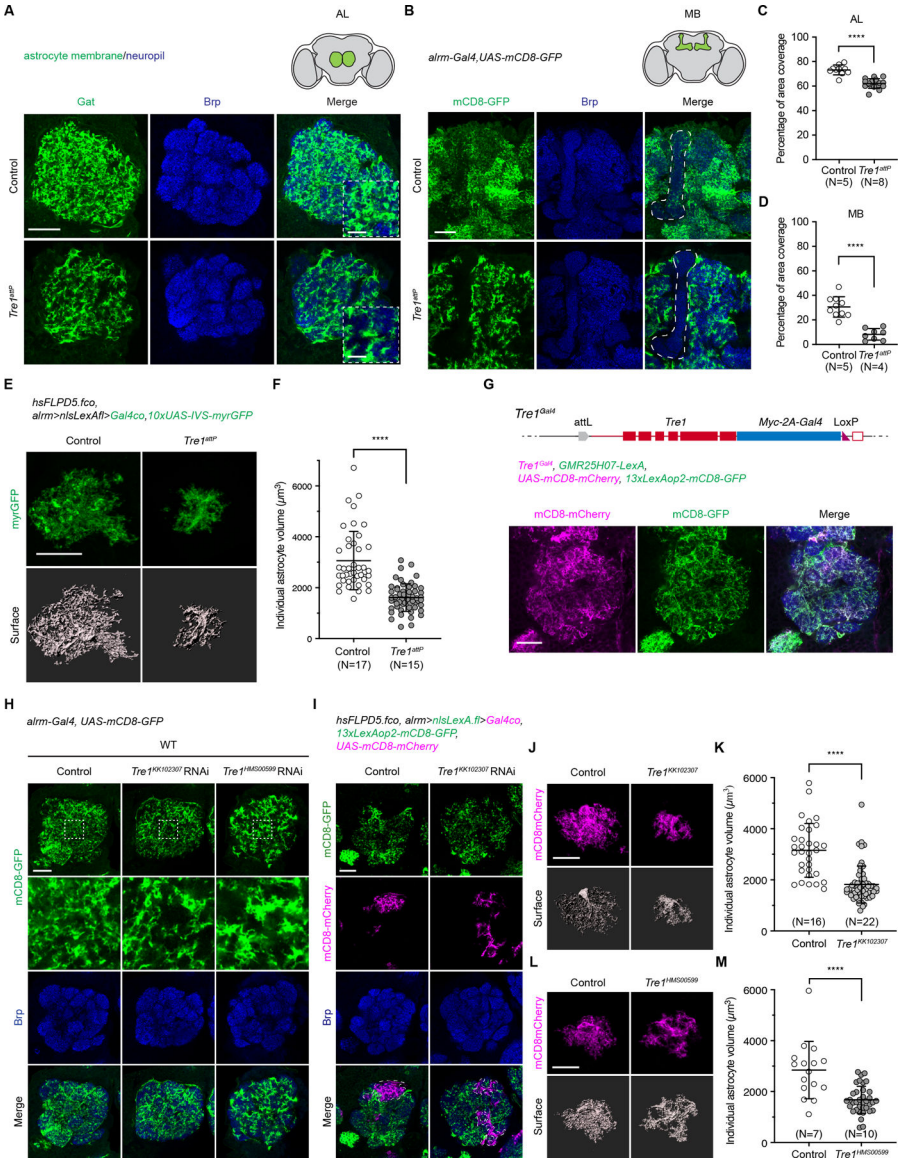

Figure 1. *Drosophila* Tre1 regulates astrocyte fine process infiltration autonomously in astrocytes

(A) Astrocytes labeled with membrane marker α-Gat antibody (green) and synaptic neuropil with α-Brp (blue) in the adult *Drosophila* brain antennal lobe (AL) in control (N=5) and *Tre1*^{attP} mutants (N=8). Insets show enlarged views to highlight the astrocyte membrane infiltration differences observed in control and *Tre1*^{attP} mutants. N, number of animals. Scale bars, 20 μm and 5 μm (insets).

(B) *alrm-Gal4 UAS-mCD8-GFP*-labeled astrocytes (green) and the neuropil (blue) in control (N=5) and *Tre1*^{attP} mutant (N=4) protocerebrum. Dashed lines mark the mushroom body.

(C) Quantification of Gat-labeled (green) astrocyte membrane coverage area percentage in the AL as shown in (A). Data points represent an independent region-of-interest (ROI) in each AL. N, number of animals. ****, p<0.0001; unpaired t test. Error bars, mean values ± S.D.

(D) Quantification of GFP-labeled (green) astrocyte membrane coverage area percentage in the MB as shown in (B). Data points represent an independent region-of-interest (ROI) in each AL. N, number of animals. ****, p<0.0001; unpaired t test. Error bars, mean values ± S.D.

(E) Images of single-cell astrocytes labeled with membrane marker myrGFP (green) using the FLP-out system and the representative IMARIS 3D-rendering surface (grey) in control and *Tre1*^{attP} mutants. Scale bar, 20 μm.

(F) Quantification of individual astrocyte volumes in control (N=17) and *Tre1*^{attP} mutants (N=15), related to (E). Data points represent single astrocytes. N, number of animals. ****, p<0.0001; unpaired t test. Error bars, mean values ± S.D.

(G) *Tre1*^{Gal4}-expressing mCD8-mCherry cell membrane (magenta) with astrocyte-specific *GMR25H07-LexA 13xLexAop2-mCD8-GFP*-labeled astrocyte membrane (green) in the ALs (N=7), and the synaptic neuropil is labeled by α-Brp (blue). N, number of animals. Scale bar, 20 μm.

(H) Images of AL astrocyte membrane surface labeled with *alrm-Gal4 UAS-mCD8-GFP* (green) and neuropil by α-Brp (blue) in control (N=9), *Tre1*^{KK102307} *RNAi* (N=10), and *Tre1*^{HMS00599} *RNAi* (N=10). N, number of animals. Scale bar, 20 μm.

(I) Images of FLP-out approach generated mosaic astrocyte clones labeled by mCD8-mCherry (magenta) in control or *Tre1*^{KK102307} *RNAi* in adjacent to neighboring WT mCD8-GFP-expressing astrocytes (green). Dashed lines mark the boundaries of mCD8-mCherry-labeled astrocytes at a single-Z plane. Representative of several experimental repeats. Scale bar, 20 μm.

(J) Images of single-cell astrocytes labeled with mCD8-mCherry (magenta) and the representative IMARIS 3D-rendering surface (grey) in control and *Tre1*^{KK102307} *RNAi*. Scale bar, 20 μm.

(K) Quantification of individual astrocyte volumes in control (N=16) and *Tre1*^{KK102307} *RNAi* (N=22), related to (J). Data points represent single astrocytes. N, number of animals. ****, p<0.0001; unpaired t test. Error bars, mean values ± S.D.

(L) Images of single-cell astrocytes labeled with mCD8-mCherry (magenta) and the representative IMARIS 3D-rendering surface (grey) in control and *Tre1*^{HMS00599} *RNAi*. Scale bar, 20 μm.

(M) Quantification of individual astrocyte volumes in control (N=7) and *Tre1*^{HMS00599} *RNAi* (N=10), related to (L). Data points represent single astrocytes. N, number of animals. ****, p<0.0001; unpaired t test. Error bars, mean values ± S.D.

See also Figure S1, S2.

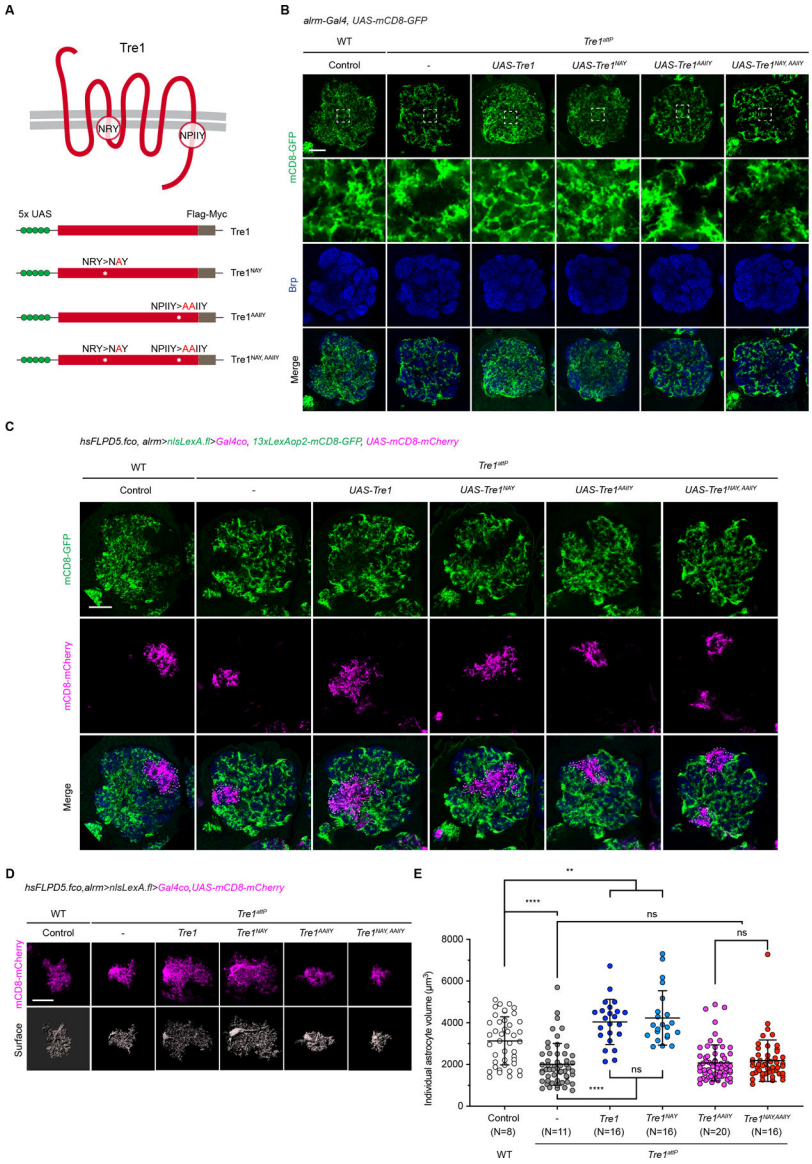

Figure 2. Tre1 controls astrocyte morphology via the NPIIY motif but not the NRY motif

(A) Schematics of Tre1 GPCR with the conserved NRY and NPIIY motifs and the *UAS*-driven transgenic constructs.

(B) Images of AL astrocytes labeled by *alrm-Gal4 UAS-mCD8-GFP* (green) and the neuropil by α-Brp (blue) in WT control (N=6) and in the $Tre1^{attP}$ mutant backgrounds either alone (N=11) or that co-express *UAS-Tre1* (N=8), $UAS\text{-}Tre1^{NAY}$ (N=8), $UAS\text{-}Tre1^{AAIIY}$ (N=11), $UAS\text{-}Tre1^{NAY,AAIIY}$ (N=10). Insets show enlarged views to highlight the astrocyte membrane infiltration differences observed in different experimental conditions. N, number of animals. Scale bars, 20 μm and 5 μm (insets).

(C) Images of astrocytes labeled by mCD8-GFP (green) with FLP-out clones expressing mCD8-mCherry (magenta) in the contexts of WT control or $Tre1^{attP}$ mutants that also express various forms of *Tre1* transgenic constructs. Dashed lines mark the boundaries

of mCD8-mCherry-labeled astrocytes at a single-Z plane. Representative of several experimental repeats. Scale bar, 20 μm.

(D) Images of single-cell astrocytes labeled with mCD8-mCherry (magenta) and the representative IMARIS 3D-rendering surface (grey) in WT control and in the *Tre1*^{attP} mutant backgrounds that express various *Tre1* transgenic constructs. Scale bar, 20 μm.

(E) Quantification of individual astrocyte volumes in the corresponding experimental conditions as shown in (D). N, number of animals. WT control, N=8; *Tre1*^{attP}, N=11; *Tre1*^{attP} + *Tre1*, N=16; *Tre1*^{attP} + *Tre1*^{NAY}, N=16; *Tre1*^{attP} + *Tre1*^{AAIIY}, N=20; *Tre1*^{attP} + *Tre1*^{NAY,AAIIY}, N=16. Data points represent single astrocytes. N, number of animals. ns, not significant; **, p<0.01; ****, p<0.0001; one-way ANOVA with multiple comparisons. Error bars, mean values ± S.D.

See also Figure S3.

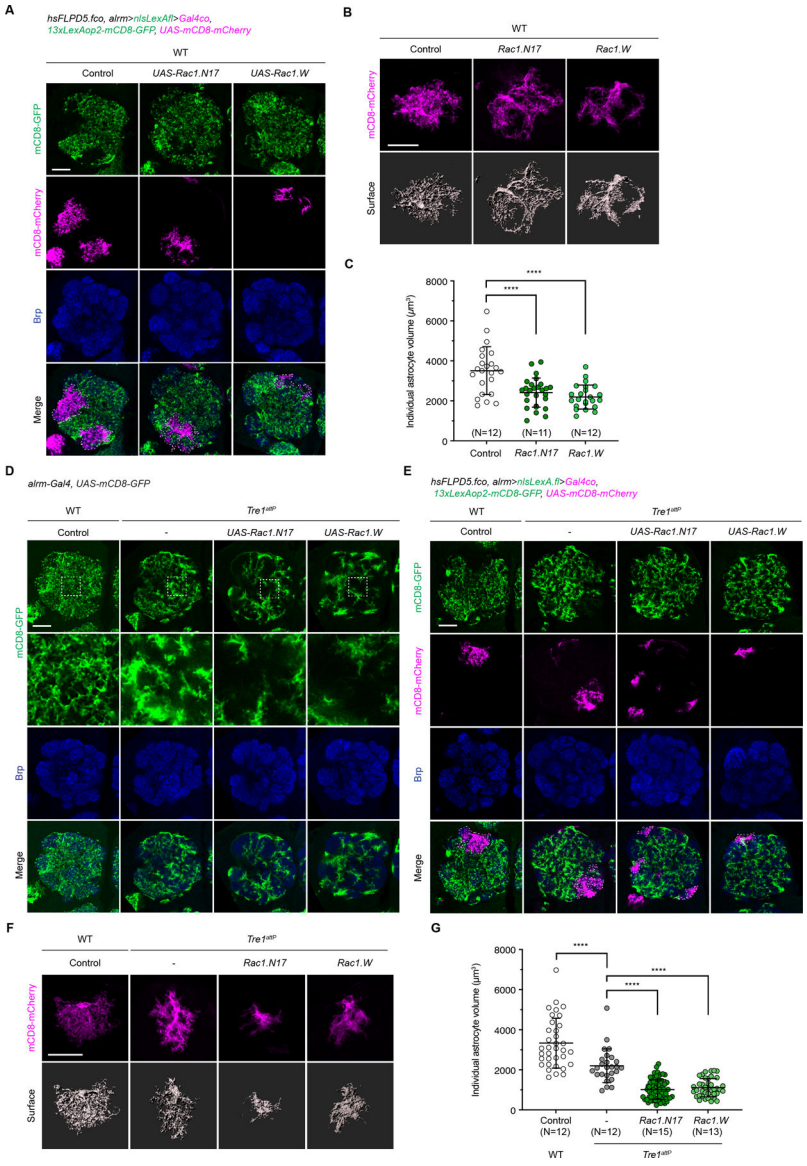

Figure 3. Tre1 balances Rac1 activity to govern proper astrocyte growth

(A) Images of astrocytes labeled by mCD8-GFP (green) with FLP-out clones expressing mCD8-mCherry (magenta) in the WT backgrounds that also express *UAS-Rac1.N17* or *UAS-Rac1.W*, and Brp labels the neuropil (blue). Dashed lines mark the boundaries of mCD8-mCherry-labeled astrocytes at a single-Z plane. Representative of several experimental repeats. Scale bar, 20 μm.

(B) Images of single-cell astrocytes labeled with mCD8-mCherry (magenta) and the representative IMARIS 3D-rendering surface (grey) in WT backgrounds that express *Rac1.N17* or *Rac1.W*. Scale bar, 20 μm.

(C) Quantification of individual astrocyte volumes in (B). Data points represent each single astrocyte. N, number of animals. WT control, N=12; *Rac1.N17*, N=11; *Rac1.W*, N=12. ****, p<0.0001; one-way ANOVA with multiple comparisons. Error bars, mean values ± S.D.

(D) Images of AL astrocyte membrane labeled with *alrm-Gal4 UAS-mCD8-GFP* (green) and neuropil with α-Brp (blue) in WT control (N=8), and in the $Tre1^{attP}$ mutant backgrounds that either alone (N=8) or co-express *UAS-Rac1.N17* (N=7), *UAS-Rac1.W* (N=8). N, number of animals. Scale bar, 20 μm.

(E) Images of astrocytes labeled by mCD8-GFP (green) with FLP-out clones expressing mCD8-mCherry (magenta) in the contexts of WT control or $Tre1^{attP}$ mutants that also express *UAS-Rac1.N17* or *UAS-Rac1.W*. Dashed lines mark the boundaries of mCD8-mCherry-labeled astrocytes at a single-Z plane. Representative of several experimental repeats. Scale bar, 20 μm.

(F) Images of single-cell astrocytes labeled with mCD8-mCherry (magenta) and the representative IMARIS 3D-rendering surface (grey) in WT control and in the $Tre1^{attP}$ mutant backgrounds that express *Rac1.N17* or *Rac1.W*. Scale bar, 20 μm.

(G) Quantification of individual astrocyte volumes in (F). Data points represent single astrocytes. N, number of animals. WT control, N=12; $Tre1^{attP}$, N=12; $Tre1^{attP}$ + *Rac1.N17*, N=15; $Tre1^{attP}$ + *Rac1.W*, N=13. ****, $p<0.0001$; one-way ANOVA with multiple comparisons. Error bars, mean values ± S.D.

See also Figure S4.

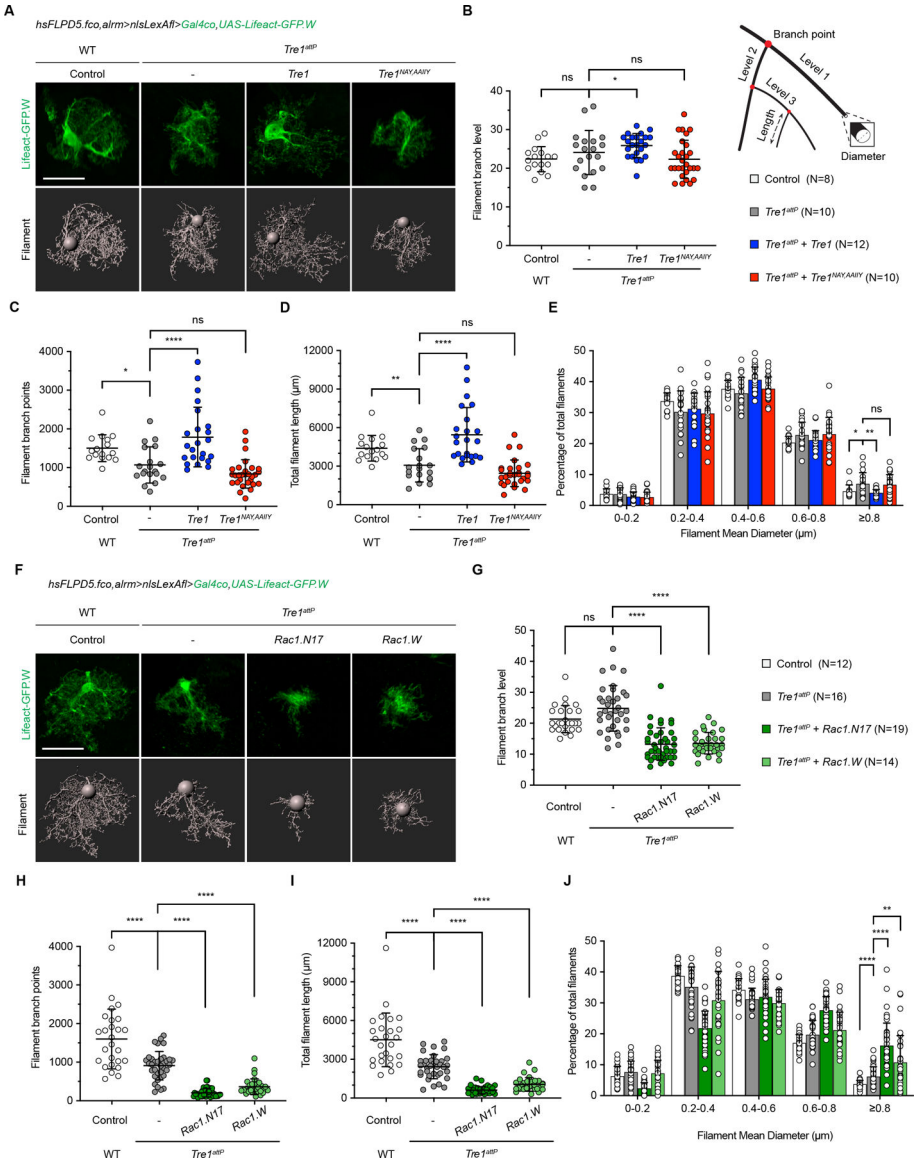

Figure 4. Tre1 regulates the actin cytoskeleton during astrocyte morphogenesis

(A) Images of single-cell astrocytes labeled with actin marker Lifeact-GFP.W (green) and the representative IMARIS 3D-rendering filament structures (grey) in WT control and in the *Tre1*^{attP} mutant backgrounds either alone or that co-express *Tre1* and *Tre1*^{NAY,AAIIY} constructs. Scale bar, 20 μm.

(B-E) Quantification of single-cell astrocyte actin cytoskeletal branch level (B), branch points (C), total length (D), and distribution of mean diameter (E) in WT control (N=8), *Tre1*^{attP} (N=10), *Tre1*^{attP} + *Tre1* (N=12), and *Tre1*^{attP} + *Tre1*^{NAY,AAIIY} (N=10), related to (A). N, number of animals. Data points represent single astrocytes. ns, not significant; *, p<0.05; **, p<0.01; ****, p<0.0001; one-way ANOVA with multiple comparisons. Error bars, mean values ± S.D.

(F) Images of single-cell astrocytes labeled with Lifeact-GFP.W (green) and the representative IMARIS 3D-rendering filament structures (grey) in WT control and in the *Tre1*^{attP} mutant backgrounds that express *Rac1.N17* or *Rac1.W*. Scale bar, 20 μm.
(G-J) Quantification of single-cell astrocyte cytoskeletal branch level (G), branch points (H), total length (I), and distribution of mean diameter (J) in WT control (N=12), *Tre1*^{attP} (N=16), *Tre1*^{attP} + *Rac1.N17* (N=19), and *Tre1*^{attP} + *Rac1.W* (N=14), related to (F). N, number of animals. Data points represent single astrocytes. ns, not significant; *, $p<0.05$; ***, $p<0.001$; ****, $p<0.0001$; one-way ANOVA with Multiple comparisons. Error bars, mean values ± S.D.
See also Figure S5, S6, and Video S1.

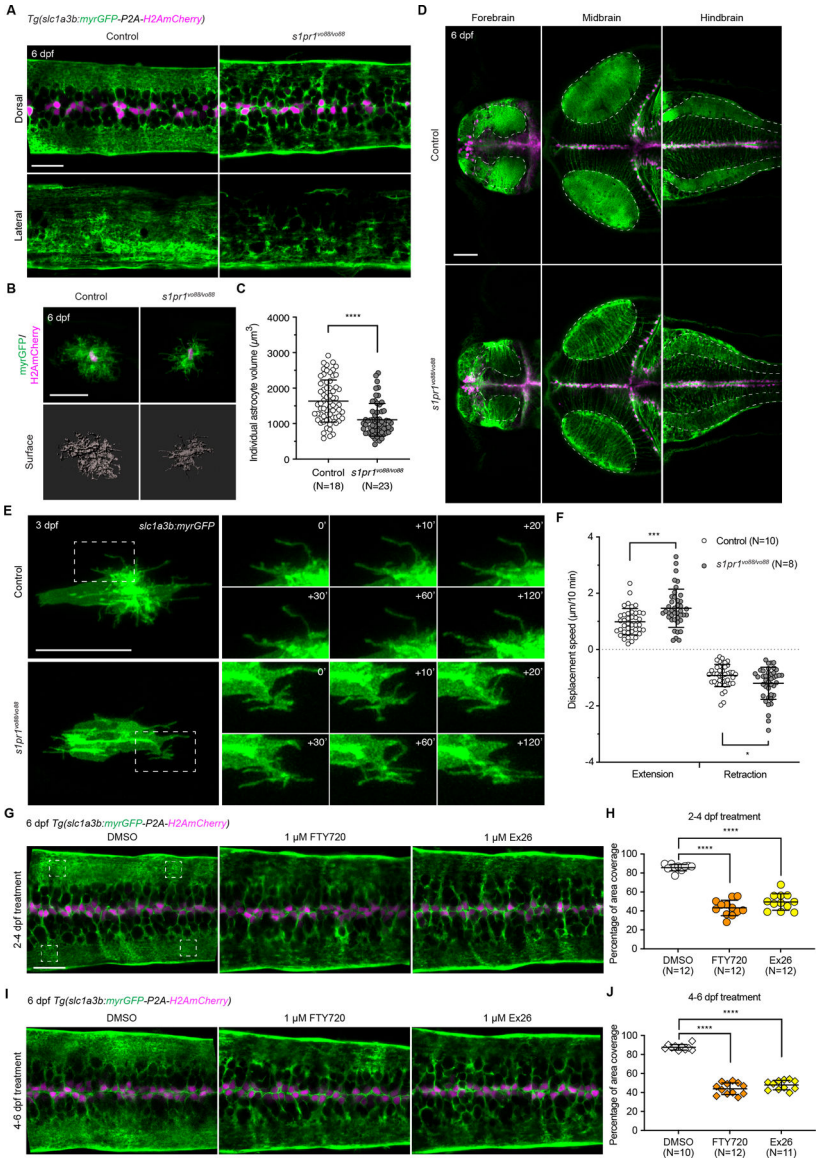

Figure 5. S1pr1 regulates astrocyte morphogenesis in zebrafish

(A) Images of spinal cord astrocyte membrane labeled with myrGFP (green) and nuclei labeled with H2AmCherry (magenta) in 6 dpf *Tg(slc1a3b:myrGFP-P2A-H2AmCherry)* transgenic control (N=15, dorsal view; N=3 lateral view) and *s1pr1*$^{vo88/vo88}$ mutants (N=17, dorsal view; N=5, lateral view). N, number of animals. Scale bar, 20 μm.

(B) Images of sparsely labeled individual astrocytes by *slc1a3b:myrGFP-P2A-H2Amcherry* DNA constructs and the representative IMARIS 3D-rendering surface (grey) at 6 dpf in the spinal cord of control and *s1pr1*$^{vo88/vo88}$ mutant zebrafish. Scale bar, 20 μm.

(C) Quantification of individual astrocyte volumes in control (N=18) and *s1pr1*$^{vo88/vo88}$ mutants (N=23) at 6 dpf, related to (B). N, number of animals. Data points represent single astrocytes. ****, $p<0.0001$; unpaired t test. Error bars, mean values ± S.D.

(D) Images of 6 dpf *Tg(slc1a3b:myrGFP-P2A-H2AmCherry)* larval brain in control (N=5) and *s1pr1*$^{vo88/vo88}$ mutants (N=6). Dashed lines mark astrocyte processes densely infiltrated neuropil in the forebrain, midbrain, and hindbrain. N, number of animals. Scale bar, 50 μm.
(E) Time-lapse still images of astrocyte process dynamics labeled with myrGFP (green) in control and *s1pr1*$^{vo88/vo88}$ mutants at 3 dpf. Dashed boxes mark the regions shown to the right. Scale bar, 20 μm.
(F) Quantification of astrocyte individual process extension and retraction displacement speed in control (N=10) and *s1pr1*$^{vo88/vo88}$ mutants (N=8) at 3 dpf. N, number of animals. Data points represent single astrocyte processes tracked. *, $p<0.05$; ***, $p<0.001$; unpaired t test. Error bars, mean values ± S.D.
(G and I) Images of 6 dpf *Tg(slc1a3b:myrGFP-P2A-H2AmCherry)* transgenic larval spinal cord astrocytes after treatment with DMSO, 1 μM FTY720, or 1 μM Ex26 at 2–4 dpf (G) or 4–6 dpf (I). Dashed boxes represent 4 independent 10 μm x 10 μm areas in the astrocyte process-enriched regions were used to quantify the GFP coverage area percentage. Scale bar, 20 μm.
(H) Quantification of relative GFP coverage area percentage at 6 dpf in the astrocyte process-enriched regions in DMSO (N=12), FTY720 (N=12), and Ex26 (N=12) after 2–4 dpf treatment. N, number of animals. Data points represent average GFP coverage area percentage of the 4 independent areas in a single fish. ****, $p<0.0001$; one-way ANOVA with multiple comparisons.
(J) Quantification of relative GFP coverage area percentage at 6 dpf in the astrocyte process-enriched regions in DMSO (N=10), FTY720 (N=12), and Ex26 (N=11) after 4–6 dpf treatment. N, number of animals. Data points represent average GFP coverage area percentage of the 4 independent areas in a single fish. ****, $p<0.0001$; one-way ANOVA with multiple comparisons.
See also Figure S7 and Video S2.

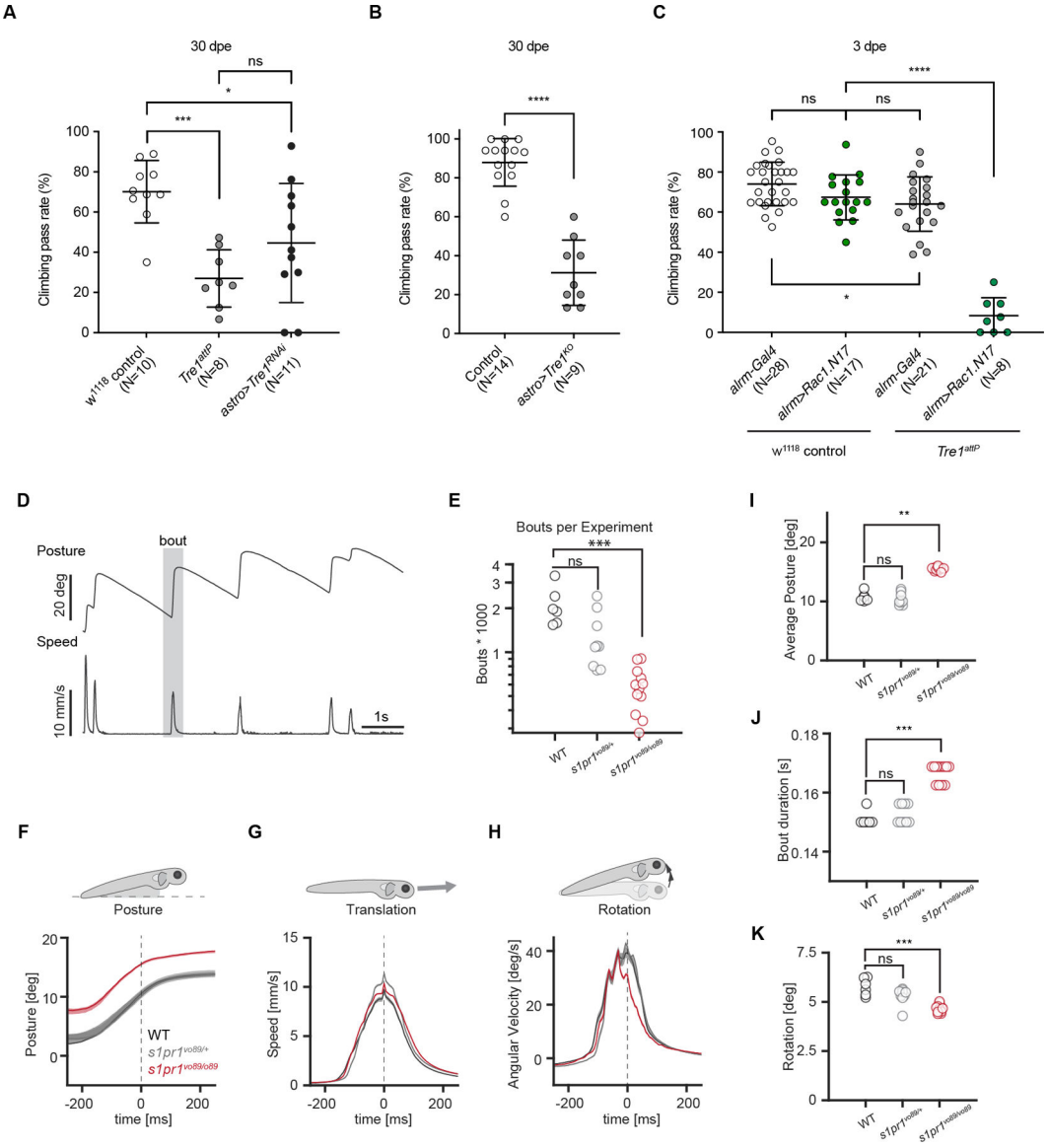

Figure 6. Loss of *Tre1*/*s1pr1* leads to behavioral deficits in *Drosophila* and zebrafish

(A) Quantification of climbing activity in w^{1118} control (N=10), $Tre1^{attP}$ mutants (N=8), and astrocyte-specific $Tre1^{HMS00599}$ RNAi flies (N=11, *alrm-Gal4 UAS-Tre1*^{HMS00599}) at 30 dpe. N, number of groups, each group contains 10–20 flies. ns, not significant; *, p<0.05; ***, p<0.001; one-way ANOVA with Multiple comparisons. Error bars, mean values ± S.D.

(B) Quantification of climbing activity in control (N=14, *alrm-Gal4 UAS-FLP*) and astrocyte-specific *Tre1* FLP-out mutants (N=9, *alrm-Gal4 UAS-FLP Tre1*^{FRT}*-Gal4*) at 30 dpe. N, number of groups, each group contains 10–20 flies. ****, p<0.0001; unpaired t test. Error bars, mean values ± S.D.

(C) Quantification of climbing activity in w^{1118} *alrm-Gal4* (N=28), w^{1118} *alrm-Gal4 UAS-Rac1.N17* (N=17), $Tre1^{attP}$ *alrm-Gal4* (N=21), and $Tre1^{attP}$ *alrm-Gal4 UAS-Rac1.N17* (N=8) at 3 dpe. N, number of groups, each group contains 10–20 flies. ns, not significant;

*, p<0.05; ****, p<0.0001; one-way ANOVA with Multiple comparisons. Error bars, mean values ± S.D.

(D) Example traces of a freely swimming zebrafish. Shaded area indicates a swim bout with postural angle shown at the top and speed over time shown in the lower traces.

(E) Quantification of bouts detected per experimental repeat for WT (N=24), *s1pr1*$^{vo89/+}$ (N=36), and *s1pr1*$^{vo89/vo89}$ fish (N=48). N, number of animals. ***, p<0.001; Kruskal-Wallis test.

(F-H) Average posture (F), speed (G), and angular velocity (H) during bout of WT, *s1pr1*$^{vo89/+}$, and *s1pr1*$^{vo89/vo89}$ fish. Dashed line indicates peak speed.

(I-K) Quantification of average posture at peak speed (I), average bout duration (J), and average total rotation (K) WT, *s1pr1*$^{vo89/+}$, and *s1pr1*$^{vo89/vo89}$ fish. **, p<0.01; ***, p<0.001; Kruskal-Wallis test.

See also Figure S8.

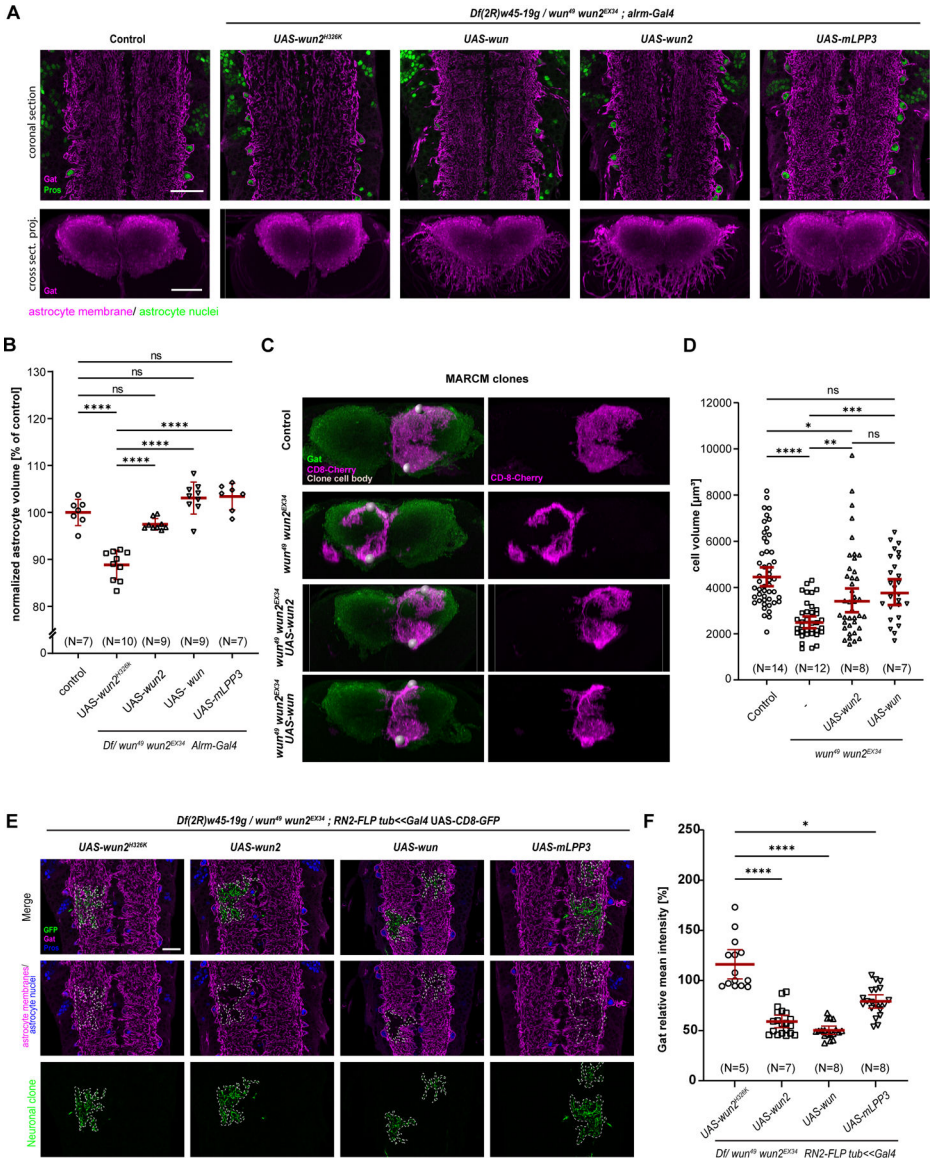

Figure 7. The *Drosophila* LPPs Wun/Wun2 control astrocyte infiltration

(A) Confocal single section images of ventral nerve cords of third instar larvae (L3) in coronal sections (upper panels) or cross-sectional 3D projections of 100 µm along the anterior-posterior axis (lower panels). Astrocyte membranes are labeled by α-Gat antibody (magenta) and nuclei labeled by α-Pros antibody (green). Scale bars, 30 µm.

(B) Quantification of normalized astrocyte infiltration volume of control (*w*^{1118}, N= 7); and *Df(2R)w45-19g* / *wun49 wun2*^{Ex34}; *alrm*-Gal4/+ animals expressing UAS-*wun2*^{H326K} (N= 10), UAS-*wun2* (N= 9), UAS-*wun* (N= 9), UAS-*mLPP3* (N= 7) related to (A). N denotes the number of animals, and individual data points represent the astrocyte volume averaged over 10 sampling volumes per larva each sized 200*100*20 pixels located in a mid-dorsal neuropil region along the a-p axis. Error bars: mean values ±SD. One-way ANOVA with multiple comparisons. ns, not significant; *, p<0.05; **, p<0.01; ***, p<0.001; ****, p<0.0001.

(C) Cross-sectional 3D projections of MARCM astrocyte clones labeled with mCD8-mCherry (magenta) and all astrocyte membrane labeled with α-Gat antibody (green) in the L3 VNC. Cell bodies of the MARCM astrocyte clones are indicated with grey spheres for clarity. Scale bar, 15 μm.

(D) Quantification of astrocyte volumes of MARCM clones for control (N= 14); wun^{49},$wun2^{EX34}$ (N= 12); wun^{49},$wun2^{EX34}$ + UAS-*wun2* (N= 8); and wun^{49},$wun2^{EX34}$ + UAS-*wun* (N= 7) related to (C). N denotes the number of animals and individual data points represent single clones. Kruskal-Wallis test with Dunn's multiple comparisons test. Error bars: mean values ± 95% CI. ns, not significant; *, p<0.05; **, p<0.01; ***, p<0.001; ****, p<0.0001.

(E) Images of L3 VNC with astrocyte membranes labeled with α-Gat (magenta) and astrocyte nuclei labeled with α-Pros (blue) in the *Df(2R)w45-19g* / wun^{49},$wun2^{EX34}$; *RN2-FLP tub<<Gal4* UAS-CD8-GFP FLP-out background expressing different *wunen* or *mLPP3* transgene in the mCD8-GFP-labeled neuronal clones (green). Dashed lines mark the boundaries of mCD8-GFP-labeled neurons at a single-Z plane. Scale bar: 20 μm.

(F) Quantification of relative α-Gat mean fluorescence intensity in the dashed line areas normalized to neighboring regions of the same size lacking a neuronal clone related to (E). UAS-$wun2^{H326K}$ (N= 5); UAS-*wun2* (N= 7); UAS-*wun* (N=8); UAS- *mLPP3* (N= 8); Kruskal-Wallis test with Dunn's multiple comparisons test. Error bars: mean values ± 95% CI. *, p<0.05; ****, p<0.0001.

See also Figure S9.

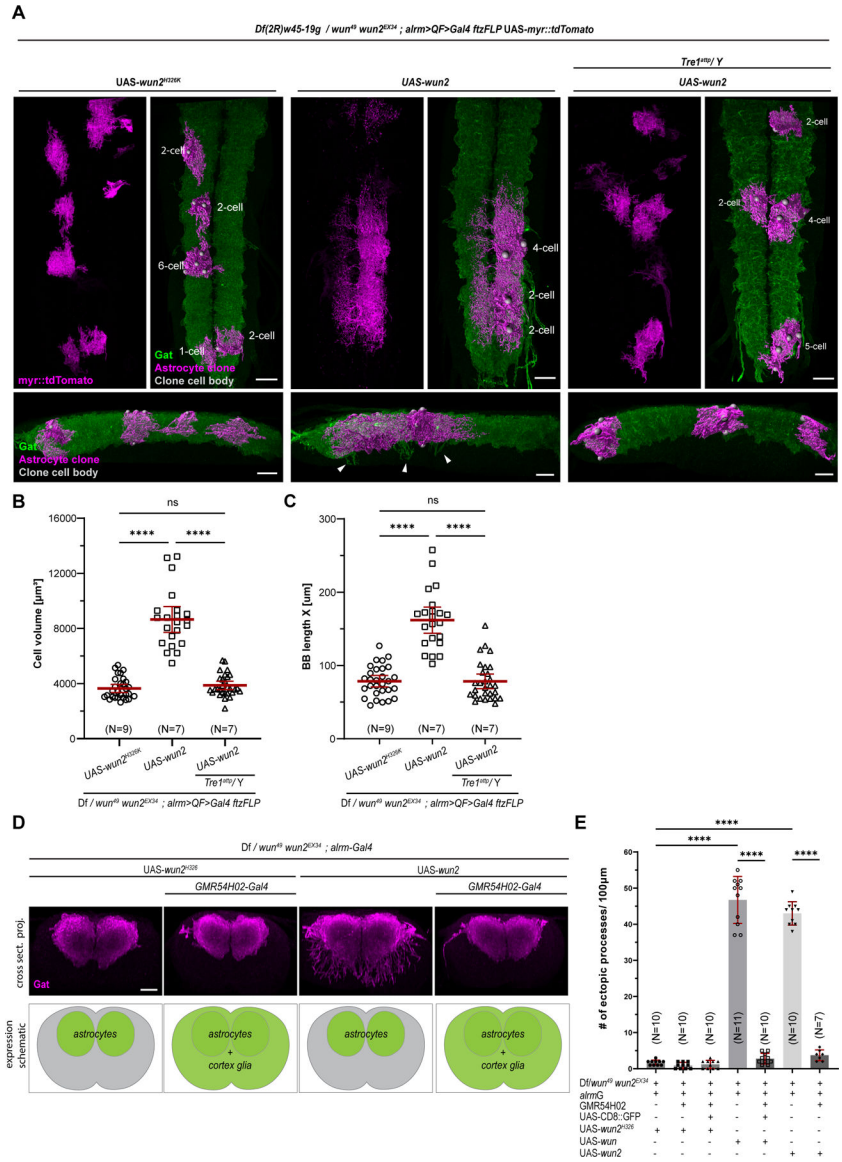

Figure 8. Wunen activity is suppressed by the loss of *Tre1*

(A) 3D projections of confocal images of astrocyte FLP-out clones labeled with myr::tdTomato (magenta) using *alrm*>QF>Gal4 *ftz*-FLP with all astrocytes labeled by α-Gat (green) in the L3 VNC. Clones also express UAS-*wun2*^{H326K} or UAS-*wun2* in either the *Df(2R)w45-19g/wun*^{49},*wun2*^{EX34} mutant background or the *Tre1*^{attP}; *Df(2R)w45-19g/wun*^{49},*wun2*^{EX34} triple mutant background. The right and bottom panels show 3D renderings of segmented astrocyte clones, and cell bodies of cells in the clone are highlighted with grey spheres for clarity. Bottom panels show a lateral view of the VNC. Arrowheads point out ectopic projections into the cortex of astrocytes adjacent to the astrocyte clones expressing UAS-*wun2*. Scale bars, 30 µm.

(B and C) Quantification of the cell volume of individual astrocytes (B) and the length of a minimal bounding box (BB) enclosing astrocyte clones (C) in UAS-*wun2*-expressing astrocytes (related to (A): *Df(2R)w45-19g/wun*^{49},*wun2*^{EX34} + UAS-*wun2*^{H326K} (N= 9);

Df(2R-w45-19g/wun^{49}*,wun2*^{EX34} + UAS-*wun2* (N= 7); and *Tre1*^{attP}*/Y*; *Df(2R)w45-19g/wun*^{49}*,wun2*^{EX34} + UAS-*wun2* (N= 7). N denotes the number of animals and individual data points represents single clones. Error bars: mean values ± 95% CI. Kruskal-Wallis test with Dunn's multiple comparisons test. ns, not significant; ****, p<0.0001.

(D) Cross-sectional 3D projections of confocal images representing 100 μm along the anterior-posterior axis of the VNC (upper panels). Astrocyte membranes are labeled by α-Gat antibody (magenta). Scale bars, 20 μm. Lower panels show a schematic representation of the expression domain in either astrocytes alone or astrocytes and cortex glia.

(E) Quantification of the number of ectopic astrocyte processes projecting from the neuropil visible in 100 μm cross-sectional 3D projections related to (D). Genotypes are indicated in the legend table. Data points represent the number of larvae tested (N=7–11). Error bars: mean values ± SD; One-way ANOVA with multiple comparisons. ****, p<0.0001.

See also Figures S10 and S11.

KEY RESOURCES TABLE

REAGENT or RESOURCE	SOURCE	IDENTIFIER
Antibodies		
Rabbit anti-Gat	Stork et al.[13]	N/A
Chicken anti-GFP	abcam	Cat# ab13970; RRID:AB_300798
Rat anti-mCherry	Thermo Fisher	Cat# M11217; RRID:AB_2536611
Rabbit anti-RFP	Rockland	Cat# 600-401-379; RRID:AB_2209751
Chicken anti-GFP	Aves	Cat# GFP-1020; RRID:AB_10000240
Mouse anti-Brp (nc82)	DSHB	Cat# nc82; RRID:AB_2314866
Mouse anti-Pro	DSHB	Cat# MR1A; RRID:AB_528440
Mouse anti-FLAG	Sigma-Aldrich	Cat# F1804; RRID:AB_262044
Mouse anti-GS (GS-6)	Sigma-Aldrich	Cat# 389M-1
Alexa Fluor 488 Donkey anti-Chicken IgG	Jackson ImmunoResearch	Cat# 703-545-155; RRID:AB_2340375
Alexa Fluor 488 Donkey anti-Rabbit IgG	Jackson ImmunoResearch	Cat# 711-545-152; RRID:AB_2313584
Alexa Fluor 488 Donkey anti-Mouse IgG	Jackson ImmunoResearch	Cat# 715-545-150; RRID:AB_2340846
Alexa Fluor 488 Donkey anti-Rat IgG	Jackson ImmunoResearch	Cat# 712-545-150; RRID:AB_2340683
Rhodamine Red-X Donkey anti-Rat IgG	Jackson ImmunoResearch	Cat# 712-295-153; RRID:AB_2340676
Rhodamine Red-X Donkey anti-Rabbit IgG	Jackson ImmunoResearch	Cat# 712-295-152; RRID:AB_2340613
Alexa Fluor 647 Donkey anti-Mouse IgG	Jackson ImmunoResearch	Cat# 715-605-151; RRID:AB_2340863
DyLight 649 Horse anti-Mouse IgG	Vector Laboratories	Cat# DI-2649; RRID:AB_2336419
DyLight 649 Goat anti-Rabbit IgG	Vector Laboratories	Cat# DI-1649; RRID:AB_2336420
HTZGFP-19C8	The Rockefeller University Bi-Institutional Antibody and Bioresource Core Facility, provided by Nathaniel Heintz	Cat# HtzGFP_02
HTZGFP-19F7	The Rockefeller University Bi-Institutional Antibody and Bioresource Core Facility, provided by Nathaniel Heintz	Cat# HtzGFP_04
Sheep anti-Digoxigenin-AP	Millipore	Cat# 11093274910; RRID:AB_514497
Chemicals, peptides, and recombinant proteins		
Ethyl 3-aminobenzoate methanesulfonate (Tricaine, MS-222)	Sigma-Aldrich	Cat# E10521
1-Phenyl 2-thiourea (PTU)	Sigma-Aldrich	Cat# P7629
Low melting agarose	Sigma-Aldrich	Cat# A9414
FTY 720	Tocris	Cat# 6176
Ex 26	Tocirs	Cat# 5833

REAGENT or RESOURCE	SOURCE	IDENTIFIER
Dimethyl Sulfoxide (DMSO)	Fisher Scientific	Cat# D159-4
16% Paraformaldehyde	Fisher Scientific	Cat# 50-980-487
Formamide	Fisher Scientific	Cat# BP228
20X SSC	Thermo Fisher	Cat# 15557044
Proteinase K	Bioline	Cat# 37084
Acetone	Fisher Scientific	Cat# A18
Triton X-100	Fisher Scientific	Cat# BP151
Tween 20	Fisher Scientific	Cat# BP337
RNase ZAP	Sigma-Aldrich	Cat#R2020
Protein G Dynalbeads	Invitrogen	Cat#10004D
Surfact-Amps NP-40	Thermo Fisher	Cat#28324
Cycloheximide	Sigma-Aldrich	Cat#01810
Emetine hydrochloride	USP	Cat#1235004
cOmplete EDTA-free protease inhibitor cocktail	Roche	Cat#11873580001
SUPERase-In RNAse inhibitor	Invitrogen	Cat#AM2694
RNase OUT ribonuclease inhibitor	Invitrogen	Cat#10777-019
DHPC	Avanti Ploar Lipids	Cat#850306P
Critical commercial assays		
HCR RNA-FISH	Molecular Instruments	N/A
Qiagen RNA minielute kit	Qiagen	Cat#74204
TruSeq Stranded protocol with ribosomal reduction	Illumina	Cat#20037135
SmartSeq Ultra Low input kit	Takara	Cat#634894
DNA Nano Prep Kit	Illumina	Cat#20015964
NGS Quantification Kit	Kapa Biosystems / Roche	Cat#KK4824
Experimental models: Organisms/strains		
Drosophila, w^{1118}	Bloomington Drosophila Stock Center	BDSC#5909; RRID:BDSC_5909
Drosophila, $Tre1^{attP}$	Bloomington Drosophila Stock Center	BDSC#84582; RRID:BDSC_84582
Drosophila, $Tre1^{\Delta EP5}$	LeBlanc et al. [28]	N/A
Drosophila, $Tre1^{sctt}$	LeBlanc et al. [28]	N/A
Drosophila, Df(2R) BSC408	Bloomington Drosophila Stock Center	BDSC#24912; RRID:BDSC_24912
Drosophila, $wun2^{N14}$	Hanyu-Nakamura et al. [63]	N/A
Drosophila, Df(2R)w45-19g	Hanyu-Nakamura et al. [63]	BDSC#6245; RRID:BDSC_6245
Drosophila, wun^{23}	Renault et al. [53]	BDSC#6951; RRID:BDSC_6951
Drosophila, wun^{9}	Renault et al. [53]	N/A
Drosophila, $wun^{49}wun2^{EX34}$	Renault et al. [78]	N/A
Drosophila, UAS-wun	Zhang et al. [27]	N/A
Drosophila, UAS-wun2-GFP	Ile et al. [79]	N/A
Drosophila, $UAS\text{-}wun2^{H326K}$	Starz-Gaiano et al. [54]	N/A
Drosophila, UAS-mLPP3	Ile et al. [79]	N/A

REAGENT or RESOURCE	SOURCE	IDENTIFIER
Drosophila, alrm-Gal4	Doherty et al. [80]	N/A
Drosophila, UAS-mCD8-GFP	Lee et al. [57]	N/A
Drosophila, Tre1^{Gal4}	This paper	N/A
Drosophila, Tre1^{FRT}-Gal4	This paper	N/A
Drosophila, UAS-TransTimer	Bloomington Drosophila Stock Center	BDSC#93411, RRID:BDSC_93411
Drosophila, hsFLPD5.fco (*hsFLPG5.PEST.Opt*)	Bloomington Drosophila Stock Center	BDSC#77140; RRID:BDSC_77140
Drosophila, alrm>nlsLexAfl>Gal4co	This paper	N/A
Drosophila, alrm>QF>Gal4	This paper	N/A
Drosophila, 10XUAS-IVS-myrGFP	Bloomington Drosophila Stock Center	BSC#32197; RRID:BDSC_32197
Drosophila, 10XUAS-IVS-myr::tdTomato	Bloomington Drosophila Stock Center	BDSC#32221; RRID:BDSC_32221
Drosophila, UAS-Lifeact-GFP.W	Bloomington Drosophila Stock Center	BDSC#57326; RRID:BDSC_57326
Drosophila, UAS-chRFP-Tub	Bloomington Drosophila Stock Center	BDSC#25773; RRID:BDSC_25773
Drosophila, UAS-mCD8-mCherry	Stork et al. [13]	N/A
Drosophila, UAS-lam-GFP	Bloomington Drosophila Stock Center	BDSC#7376; RRID:BDSC_7376
Drosophila, GMR25H07-Gal4	Bloomington Drosophila Stock Center	BDSC#49145; RRID:BDSC_49145
Drosophila, GMR25H07-LexA	Bloomington Drosophila Stock Center	BDSC#52711; RRID:BDSC_52711
Drosophila, GMR54H02-Gal4	Bloomington Drosophila Stock Center	BDSC#45784; RRID:BDSC_45784
Drosophila, 13xLexAop2-mCD8-GFP	Bloomington Drosophila Stock Center	BDSC#32203; RRID:BDSC_32203
Drosophila, UAS-Tre1^{KK102307}	Vienna Drosophila Resource enter	V108952
Drosophila, UAS-Tre1^{HMS00599}	Bloomington Drosophila Stock Center	BDSC#33718; RRID:BDSC_33718
Drosophila, 5xUAS-Tre1	This paper	N/A
Drosophila, 5xUAS-Tre1^{NAY}	This paper	N/A
Drosophila, 5xUAS-Tre1^{AAIIY}	This paper	N/A
Drosophila, 5xUAS-Tre1^{NAY,AAIIY}	This paper	N/A
Drosophila, UAS-Rac1.N17	Bloomington Drosophila Stock Center	BDSC#6292; RRID:BDSC_6292
Drosophila, UAS-Rac1.W	Bloomington Drosophila Stock Center	BDSC#28874; RRID:BDSC_28874
Drosophila, RN2-FLP tub-Gal4 UAS-mCD8-GFP	Ou et al. [59]	N/A
Drosophila, n-syb-Gal4	Rao et al. [58]	N/A
Drosophila, elav-Gal80	Yang et al. [89]	N/A
Drosophila, alrm-Gal4, UAS-EGFP-L10a	Huang et al. [90]	N/A
Zebrafish, *gpr84^{vo87}*	This paper	N/A
Zebrafish, *s1pr1^{vo88}*	This paper	N/A
Zebrafish, *s1pr1^{vo89}*	This paper	N/A
Zebrafish, *Tg(slc1a3b:myrGFP-P2A-H2AmCherry)*	Chen et al. [16]	ZFIN: ZDB-ALT-200915-2
Oligonucleotides		
See Table S1.	N/A	N/A
Recombinant DNA		
pBsk-attB-Tre1-Gal4	This paper	N/A

REAGENT or RESOURCE	SOURCE	IDENTIFIER
pBsk-attB-FRT-Tre1-FRT-Gal4	This paper	N/A
pattB-5xUAS-Tre1	This paper	N/A
pattB-5xUAS-Tre1 ^{NAY}	This paper	N/A
pattB-,5xUAS-Tre1 ^{AAIIY}	This paper	N/A
pattB-5xUAS-Tre1 ^{NAY,AAIIY}	This paper	N/A
pCaSpeR-EFAN-alrm-QNUG	This paper	N/A
gcm-FLP	This paper	N/A
ftz-FLP	This paper	N/A
Software and algorithms		
Zen	Zeiss	https://www.zeiss.com/microscopy/en/products/software/zeiss-zen.html
IMARIS 9	Bitplane	https://imaris.oxinst.com/versions/9
Slidebook	Innovative Imaging Innovations (3i)	https://www.intelligent-imaging.com/slidebook
Fiji (ImageJ)	ImageJ	https://imagej.net/software/fiji/
Prism 8/9	GraphPad	https://www.graphpad.com/
FlyTracker	Alvarez-Salvado et al. [51]	https://github.com/nagellab/AlvarezSalvado_ElementaryTransformations
SAMPL	Zhu et al. [52]	https://osf.io/wjh25/
Bcl2FastQ	Illumina	N/A
Matlab	Mathworks	N/A
Other		
Confocal Microscope LSM880 or LSM 980 Airyscan	Zeiss	N/A
spinning-disk confocal microscope equipped with a Yokogawa CSX-X1 scan head	Innovative Imaging Innovations (3i)	N/A